

# A Unified Two-Stage Generative Diffusion Framework for Channel Estimation and Port Selection in Multiuser MIMO-FAS

Erqiang Tang, Wei Guo, *Member, IEEE*, Hengtao He, *Member, IEEE*, Shenghui Song, *Senior Member, IEEE*, Jun Zhang, *Fellow, IEEE*, and Khaled B. Letaief, *Fellow, IEEE*

**Abstract**—Fluid antenna systems (FAS) have emerged as a promising technology for next-generation wireless systems. However, practical multiuser multiple-input multiple-output FAS (MIMO-FAS) faces two inherently coupled challenges: acquiring accurate high-dimensional channel state information (CSI) from limited RF chains and solving the combinatorial port selection problem, where the effectiveness of the latter highly depends on the result of the former. In this paper, we propose a unified two-stage diffusion framework that formulates the joint task as a maximum-a-posteriori (MAP) inference problem and decomposes it into two sequential sampling stages through a plug-in approximation. For Stage I, a continuous flow-based diffusion model serves as a powerful implicit prior for 2D FAS channels, and a parallel guided generation scheme realizes approximate posterior sampling, enabling accurate multiuser channel recovery even under severely low sub-sampling ratios. For Stage II, a discrete diffusion model is trained to approximate the conditional port selection distribution by combining supervised learning on heuristic labels with reinforcement fine-tuning, effectively overcoming the local optima of conventional heuristic algorithms. Extensive simulations demonstrate that the proposed framework simultaneously achieves exceptional channel estimation accuracy and globally optimized port selection, substantially improving the minimum achievable rate.

**Index Terms**—Channel Estimation, Diffusion Model, Fluid Antenna Systems (FAS), Multiple Access

## I. INTRODUCTION

**D**RIVEN by the proliferation of edge devices and wireless applications, the forthcoming sixth-generation (6G) wireless networks are anticipated to offer tremendous data rates, ultra-low latency, and robust reliability [1], [2]. To satisfy these stringent requirements, massive multiple-input multiple-output (MIMO) has been widely regarded as a key enabling technology [3]. However, as conventional MIMO architectures scale up to accommodate the next-generation demands, they encounter two fundamental challenges. First, equipping extremely large antenna arrays with a massive number of radio frequency (RF) chains imposes prohibitive hardware costs and significant power consumption [4]. Second, conventional MIMO systems rely on fixed-position antenna (FPA) arrays that are constrained by the half-wavelength antenna spacing rule. This fixed arrangement restricts their capability to fully exploit the spatial variations inherent in wireless channels,

thereby limiting the overall system performance in terms of diversity and/or multiplexing gains [5].

To address these limitations, the fluid antenna system (FAS) has recently been proposed [6], [7]. Conceptually, FAS encompasses any form of movable or non-movable antennas that are capable of reconfiguring their positions. The possibility of adjusting antenna positions (also referred to as ‘ports’) provides additional degrees of freedom (DoF) in space, thus allowing FAS to better explore the spatial diversity within a predefined region.

While initial investigations on FAS mainly focused on single-input single-output (SISO) setups where only a single port is activated [8]–[11], FAS and MIMO are not mutually exclusive [12]. The integration of these two paradigms, termed MIMO-FAS, can be realized by connecting a massive number of densely packed ports, which enable fine-grained spatial reconfigurability, to a substantially smaller number of RF chains for simultaneous multi-port activation. This dynamic multi-port reconfigurability enables MIMO-FAS to proactively shape the channel matrix into more favorable realizations, yielding significant rate improvements compared to conventional FPA-based MIMO [13]. In multiuser scenarios, such position flexibility is particularly promising: optimizing the channel matrix corresponds to repositioning the fluid antennas to escape from both deep fades and interference, effectively delivering considerable spatial multiplexing gains without escalating hardware complexity [14], [15].

### A. Prior Work

Fully unlocking the potential of multiuser MIMO-FAS requires both accurate channel state information (CSI) acquisition and subsequent port selection (also known as ‘antenna position optimization’). Fundamentally, the effectiveness of port selection hinges on the quality of the acquired CSI, as estimation errors translate directly into suboptimal port decisions. Despite this inherent coupling, existing literature largely treats these two tasks in isolation [14], [16]–[29]: available channel estimators are developed independently of downstream objectives, while most port selection algorithms assume the availability of perfect CSI. In practical deployments, this decoupled treatment inevitably results in a cascading performance degradation.

Channel estimation for FAS is highly challenging: an extremely high-dimensional channel matrix must be recovered from a small number of port observations, and accumulating sufficient observations inevitably incurs a substantial switching

Erqiang Tang, Wei Guo, Shenghui Song, Jun Zhang, and Khaled B. Letaief are with the Department of Electronic and Computer Engineering, The Hong Kong University of Science and Technology (HKUST), Hong Kong. Emails: etangaa@connect.ust.hk, {eweigu, eeshsong, eejzhang, eekhaled}@ust.hk.

Hengtao He is with the National Mobile Communications Research Laboratory, Southeast University, Nanjing, China. Email: hehengtao@seu.edu.cn.

cost. Most existing works tackled this problem in SISO scenarios, leveraging either the intrinsic channel sparsity via compressed sensing (CS)-based methods [16]–[18] or the spatial correlation among densely deployed FAS ports [19]–[21]. However, CS-based approaches suffer from an extremely singular measurement matrix when formulated over high-resolution angular dictionaries, which degrades the estimation accuracy [22]. Moreover, while the switching cost of these approaches might be acceptable for SISO-FAS, it becomes prohibitive when extended to multiuser MIMO-FAS, where the observation burden aggregates across multiple users and severely restricts system scalability. In the multiuser context, a low-sample-size sparse channel recovery (L3SCR) framework was proposed in [23] to specifically tackle FAS-aided multiuser uplink channel estimation. However, this method strictly relies on complete array observations at the BS.

The quality of the acquired CSI directly determines the effectiveness of the subsequent port selection. Despite this dependency, prior studies have extensively investigated the joint design of antenna positioning and beamforming/combining largely in isolation from the channel estimation process, typically assuming either perfect CSI or imperfect CSI with fixed statistical estimation errors [14], [28], [29]. These works targeted diverse objectives, such as total transmit power minimization [14], [24], [27], sum-rate maximization [25], [26], and max-min fairness [28]. Due to the coupled optimization variables and non-convex objectives, existing approaches typically resort to suboptimal solutions, either via alternating optimization (AO) techniques [24], [25], [27] or heuristic antenna positioning, such as multi-directional descent (MDD) [14] and particle swarm optimization (PSO) [28], under fixed beamforming/combining. However, these iterative methods are prone to being trapped in local optima. Although a recent work [29] achieved jointly optimal beamforming and antenna positioning under discrete antenna movements, its prohibitive computational complexity renders it unscalable for high-dimensional FAS. Consequently, the existing literature lacks a unified framework for multiuser MIMO-FAS that jointly accounts for channel estimation and port selection under practical conditions.

## B. Contributions

In this paper, we propose a unified two-stage framework driven by generative diffusion models to systematically address both channel estimation and port selection in multiuser MIMO-FAS scenarios. Unlike conventional decoupled designs, the two stages in our framework are not independently considered. Instead, they are rigorously derived from a single maximum-a-posteriori (MAP) inference problem over the channel latent variable, which subsequently decomposes into two sequential sampling stages via a plug-in approximation. In each stage, a dedicated diffusion model is employed to facilitate the approximation of and sampling from the target distribution. Aligned with realistic hardware implementations, we focus on a two-dimensional (2D) discrete FAS architecture [30]–[32]. The main contributions of this paper are summarized as follows:

- First, we establish a comprehensive system model for

the uplink multiuser MIMO-FAS system, characterizing the high-dimensional 2D FAS channel via multi-path propagation modeling, the sparse spatial sampling model for pilot observation, and the port selection-dependent effective channel for multiuser data reception. On this basis, we develop a unified probabilistic formulation that casts the joint channel estimation and port selection task as a single MAP inference problem  $\arg \max_{\mathbf{x}} p(\mathbf{x}|\mathbf{Y}_p)$ , where the complete channel serves as a latent variable. By analyzing the intractability of this joint posterior, we motivate a plug-in approximation that naturally gives rise to the proposed two-stage framework.

- For Stage I, which aims to accurately reconstruct the channel from extremely limited observations, we exploit a flow-based diffusion model [33] trained via the flow matching framework [34]–[36] to serve as a powerful learned implicit prior for 2D FAS channels. To enable simultaneous multiuser channel estimation, we develop a guided generation mechanism inspired by the flow-driven posterior sampling (FlowDPS) solver for inverse problems [37], effectively realizing approximate sampling from the channel posterior established in the proposed probabilistic formulation. Numerical experiments show that our proposed estimator achieves remarkable accuracy with only 20 inference steps and maintains exceptional robustness even under severely low sub-sampling ratios, significantly outperforming conventional baselines.
- For Stage II, we employ a discrete diffusion model to approximate the conditional port selection distribution established in the proposed probabilistic formulation. The model is trained to maximize the expected utility, starting from a foundation model via supervised training on sub-optimal heuristic labels, followed by a reinforcement fine-tuning stage that leverages the inherent generative stochasticity to actively explore the combinatorial search space and overcome the local optima of conventional heuristic algorithms. Simulation results show that our proposed unified two-stage diffusion framework simultaneously achieves accurate channel recovery and globally-aware port selection, resulting in a significant improvement in the minimum achievable rate.

The remainder of this paper is organized as follows. Section II presents the system model and develops the unified probabilistic formulation that motivates the two-stage decomposition. Section III details the proposed flow-based diffusion framework for Stage I channel posterior sampling. Section IV develops a discrete diffusion-based solver for Stage II conditional port selection. Finally, Section V evaluates the performance of the proposed unified framework via numerical simulations, and Section VI concludes the paper.

*Notations:*  $a$ ,  $\mathbf{a}$ ,  $\mathbf{A}$ , and  $\mathcal{A}$  represent a scalar, a vector, a matrix, and a set, respectively.  $\mathbb{R}^{M \times N}$  and  $\mathbb{C}^{M \times N}$  denote the sets of real and complex matrices of dimension  $M \times N$ , respectively.  $(\cdot)^T$ ,  $(\cdot)^H$ ,  $(\cdot)^{-1}$ , and  $(\cdot)^\dagger$  denote the transpose, conjugate transpose, inverse, and Moore-Penrose pseudo-inverse, respectively.  $\text{vec}(\mathbf{A})$  denotes the vectorization of matrix  $\mathbf{A}$ .  $\Re(\cdot)$  and  $\Im(\cdot)$  denote the real and imaginary

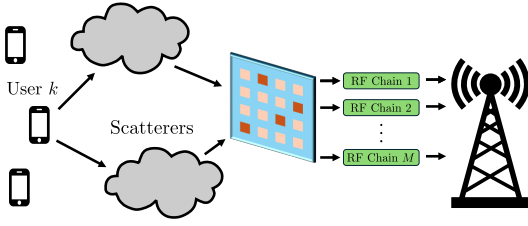


Fig. 1. An illustration of the multiuser MIMO-FAS system model.

parts of a complex variable, respectively.  $\otimes$  represents the Kronecker product.  $|\mathcal{A}|$  represents the cardinality of set  $\mathcal{A}$ .  $\|\mathbf{a}\|_1$ ,  $\|\mathbf{a}\|_2$ , and  $\|\mathbf{A}\|_F$  represent the  $\ell_1$ -norm,  $\ell_2$ -norm, and Frobenius norm, respectively.  $[\mathbf{a}]_{i:j}$  denotes the slicing operation, extracting the  $i$ -th through  $j$ -th entries of vector  $\mathbf{a}$ .  $\mathbb{E}[\cdot]$  denotes the expected value of a random variable/vector.  $\mathbf{I}_N$  denotes the identity matrix with size  $N \times N$ .  $\mathcal{CN}(\mathbf{a}, \mathbf{A})$  denotes the circularly symmetric complex Gaussian (CSCG) distribution with mean vector  $\mathbf{a}$  and covariance matrix  $\mathbf{A}$ .  $D_{\text{KL}}(p \parallel q)$  denotes the Kullback-Leibler (KL) divergence between probability distributions  $p$  and  $q$ .

## II. SYSTEM MODEL AND PROBLEM FORMULATION

### A. Channel Model

As illustrated in Fig. 1, we consider an uplink multiuser wireless communication system where a base station (BS) equipped with a 2D FAS serves  $K$  single-FPA users. The FAS features a rectangular surface of dimensions  $W = W_x \lambda \times W_y \lambda$ , with  $\lambda$  being the carrier wavelength. This surface is uniformly partitioned into a grid of  $N = N_x \times N_y$  discrete candidate ports. To enable spatial multiplexing of the  $K$  users, the BS incorporates  $M$  RF chains ( $N \gg M \geq K$ ), each connected to a dedicated fluid antenna that can dynamically switch among the  $N$  ports.

Let  $\mathbf{H}_k \in \mathbb{C}^{N_x \times N_y}$  denote the complete uplink CSI matrix from user  $k$  to all FAS ports at the BS. To characterize the multi-path propagation environment, we consider a finite scattering channel model [15]. Under this model, assuming the wireless channel is composed of  $N_p$  dominant paths, the complex channel matrix  $\mathbf{H}_k$  can be formulated as

$$\mathbf{H}_k = \sqrt{\frac{1}{N_p}} \sum_{i=1}^{N_p} g_{k,i} \mathbf{a}_x(\theta_{k,i}, \phi_{k,i}) \mathbf{a}_y(\theta_{k,i}, \phi_{k,i})^T, \quad (1)$$

where  $g_{k,i}$  corresponds to the complex baseband gain of the  $i$ -th propagation path for user  $k$ , while  $\theta_{k,i}$  and  $\phi_{k,i}$  represent the associated elevation and azimuth angles-of-arrival (AoAs), respectively. Furthermore, the receive steering vectors along the horizontal (x-axis) and vertical (y-axis) dimensions, denoted by  $\mathbf{a}_x(\theta, \phi)$  and  $\mathbf{a}_y(\theta, \phi)$ , are respectively given by<sup>1</sup>

$$\begin{aligned} \mathbf{a}_x(\theta, \phi) &= \left[ 1, e^{-j2\pi \frac{W_x}{N_x-1} \cos \theta \sin \phi}, \dots, e^{-j2\pi W_x \cos \theta \sin \phi} \right]^T, \\ \mathbf{a}_y(\theta, \phi) &= \left[ 1, e^{-j2\pi \frac{W_y}{N_y-1} \sin \theta}, \dots, e^{-j2\pi W_y \sin \theta} \right]^T. \end{aligned} \quad (2)$$

<sup>1</sup>Although the vertical steering vector  $\mathbf{a}_y$  depends only on the elevation angle  $\theta$ , the azimuth angle  $\phi$  is still kept in the argument to maintain notational symmetry with  $\mathbf{a}_x$ .

### B. Signal Model

The uplink communication is structured into two consecutive phases: a pilot transmission phase for channel observation, followed by a data transmission phase in which the BS selects a subset of  $M$  ports for signal reception.

During the pilot transmission phase, the  $K$  users synchronously transmit mutually orthogonal pilot sequences, defined by a codebook matrix  $\mathbf{P} \in \mathbb{C}^{K \times K}$  satisfying  $\mathbf{P}\mathbf{P}^H = \mathbf{I}_K$ , to prevent inter-user interference. Constrained by the  $M$  RF chains, only  $M$  ports can be observed simultaneously. To accumulate sufficient spatial observations across the  $N$  candidate ports, the pilot block is repeatedly transmitted over  $L$  consecutive cycles, with a different subset of  $M$  ports activated in each cycle. Over the  $L$  cycles, a total of  $N_{\mathcal{O}} = LM$  port observations are collected, yielding a sub-sampling ratio of  $\delta = N_{\mathcal{O}}/N$ . Let  $\mathcal{O} \subset \{1, \dots, N\}$  denote the ordered index set of the sampled ports across all cycles, where  $|\mathcal{O}| = N_{\mathcal{O}}$ . The overall spatial sampling process can then be represented by a binary selection matrix  $\mathbf{\Omega}_{\mathcal{O}} \in \{0, 1\}^{N_{\mathcal{O}} \times N}$ , whose rows are selected from  $\mathbf{I}_N$  according to the indices in  $\mathcal{O}$ .

By stacking the received pilot signals from all  $L$  cycles, the aggregated received signal matrix  $\mathbf{Y}_p \in \mathbb{C}^{N_{\mathcal{O}} \times K}$  at the BS is given by

$$\mathbf{Y}_p = \mathbf{\Omega}_{\mathcal{O}} \tilde{\mathbf{H}} \mathbf{P} + \mathbf{N}, \quad (3)$$

where  $\tilde{\mathbf{H}} = [\tilde{\mathbf{h}}_1, \tilde{\mathbf{h}}_2, \dots, \tilde{\mathbf{h}}_K] \in \mathbb{C}^{N_{\mathcal{O}} \times K}$  represents the concatenated complete CSI matrix for all  $K$  users, with  $\tilde{\mathbf{h}}_k = \text{vec}(\mathbf{H}_k)$  being the vectorized channel of user  $k$ . Here,  $\mathbf{N} \in \mathbb{C}^{N_{\mathcal{O}} \times K}$  denotes the received additive white Gaussian noise (AWGN) matrix, whose entries are independent and identically distributed (i.i.d.) according to  $\mathcal{CN}(0, \sigma_n^2)$ .

To facilitate learning-based signal processing, we define a real-valued equivalent representation for each user's channel, denoted by  $\mathbf{h}_k$ . Specifically, we introduce an isomorphic mapping  $f : \mathbb{C}^{N \times 1} \rightarrow \mathbb{R}^{2N \times 1}$  that converts the complex channel vectors to their real-valued counterparts. Accordingly,  $\mathbf{h}_k$  can be expressed as

$$\mathbf{h}_k = f(\tilde{\mathbf{h}}_k) = \begin{bmatrix} \Re(\tilde{\mathbf{h}}_k) \\ \Im(\tilde{\mathbf{h}}_k) \end{bmatrix}. \quad (4)$$

The corresponding inverse mapping, denoted by  $f^{-1} : \mathbb{R}^{2N \times 1} \rightarrow \mathbb{C}^{N \times 1}$ , does the opposite by mapping the real-valued network outputs back to the complex domain, i.e.,

$$\tilde{\mathbf{h}}_k = f^{-1}(\mathbf{h}_k) = [\mathbf{h}_k]_{1:N} + j[\mathbf{h}_k]_{N+1:2N}. \quad (5)$$

As a result, the complete multiuser channel matrix  $\tilde{\mathbf{H}}$  can be explicitly written in terms of the real-valued individual channel vectors as

$$\tilde{\mathbf{H}} = [f^{-1}(\mathbf{h}_1), f^{-1}(\mathbf{h}_2), \dots, f^{-1}(\mathbf{h}_K)]. \quad (6)$$

In the data transmission phase, the BS activates  $M$  out of the  $N$  candidate ports for uplink data reception. Mathematically, we represent the port selection decision by a binary mask  $\mathbf{x} \in \{0, 1\}^N$  with  $\|\mathbf{x}\|_1 = M$ , where  $x_i = 1$  indicates that the  $i$ -th port is activated, and  $x_i = 0$  otherwise. The corresponding port selection matrix  $\mathbf{\Omega}_{\mathbf{x}} \in \{0, 1\}^{M \times N}$  is formed by extracting the rows of  $\mathbf{I}_N$  indexed by the nonzero entries of  $\mathbf{x}$ , which yields

the effective multiuser channel

$$\tilde{\mathbf{H}} = \mathbf{\Omega}_x \tilde{\mathbf{H}} \in \mathbb{C}^{M \times K}. \quad (7)$$

The baseband received signal at the BS is then given by

$$\mathbf{y}_d = \tilde{\mathbf{H}}\mathbf{s} + \mathbf{n}_d, \quad (8)$$

where  $\mathbf{s} \in \mathbb{C}^{K \times 1}$  represents the transmitted data symbol vector from all  $K$  users with normalized signal power  $\mathbb{E}[\mathbf{s}\mathbf{s}^H] = \mathbf{I}_K$ , and  $\mathbf{n}_d \sim \mathcal{CN}(\mathbf{0}, \sigma_n^2 \mathbf{I}_M)$  is the AWGN vector.

### C. Problem Formulation

For uplink signal detection, a linear receive combining scheme is adopted at the BS. With a combining matrix  $\mathbf{W} \in \mathbb{C}^{M \times K}$ , the decoded data vector is given by  $\hat{\mathbf{s}} = \mathbf{W}^H \mathbf{y}_d$ . To simplify our analysis and focus purely on the port selection design, we adopt the minimum mean squared error (MMSE) receiver [38]. Given perfect knowledge of the complete channel  $\tilde{\mathbf{H}}$ , the MMSE combining matrix is given by

$$\mathbf{W}_{\text{MMSE}}(\mathbf{x}, \tilde{\mathbf{H}}) = \left( \mathbf{\Omega}_x \tilde{\mathbf{H}} \tilde{\mathbf{H}}^H \mathbf{\Omega}_x^T + \sigma_n^2 \mathbf{I}_M \right)^{-1} \mathbf{\Omega}_x \tilde{\mathbf{H}}. \quad (9)$$

Let  $\mathbf{w}_k(\mathbf{x}, \tilde{\mathbf{H}})$  and  $\bar{\mathbf{h}}_k$  denote the  $k$ -th columns of  $\mathbf{W}_{\text{MMSE}}(\mathbf{x}, \tilde{\mathbf{H}})$  and the true effective channel  $\tilde{\mathbf{H}}$ , respectively. The corresponding receive signal-to-interference-plus-noise ratio (SINR) for user  $k$  is expressed as

$$\gamma_k(\mathbf{x}, \tilde{\mathbf{H}}) = \frac{|\mathbf{w}_k(\mathbf{x}, \tilde{\mathbf{H}})^H \bar{\mathbf{h}}_k|^2}{\sum_{j \neq k} |\mathbf{w}_k(\mathbf{x}, \tilde{\mathbf{H}})^H \bar{\mathbf{h}}_j|^2 + \sigma_n^2 \|\mathbf{w}_k(\mathbf{x}, \tilde{\mathbf{H}})\|_2^2}, \quad (10)$$

with the achievable rate for user  $k$  given by

$$R_k(\mathbf{x}, \tilde{\mathbf{H}}) = \log_2(1 + \gamma_k(\mathbf{x}, \tilde{\mathbf{H}})). \quad (11)$$

To ensure performance fairness among all active users, our objective is to optimize the port selection strategy  $\mathbf{x}$  by maximizing the minimum achievable rate, subject to FAS hardware constraints. The corresponding max-min optimization problem can be formulated as

$$\max_{\mathbf{x}} \min_{k \in \{1, \dots, K\}} R_k(\mathbf{x}, \tilde{\mathbf{H}}) \quad (12a)$$

$$\text{s.t. } \mathbf{x} \in \{0, 1\}^N, \quad (12b)$$

$$\|\mathbf{x}\|_1 = M. \quad (12c)$$

Directly solving problem (12) in practice is intractable due to two fundamental challenges. First, the objective relies on the complete true channel  $\tilde{\mathbf{H}}$ , which is inaccessible at the BS since only the highly sub-sampled pilot signals  $\mathbf{Y}_p$  are observed. Second, even if  $\tilde{\mathbf{H}}$  were perfectly known, optimizing the discrete binary mask  $\mathbf{x}$  poses an NP-hard combinatorial optimization (CO) problem. Finding the optimal solution via exhaustive search requires evaluating  $\binom{N}{M}$  possible combinations, which incurs a prohibitive computational burden for large-scale FAS.

To circumvent these challenges, we adopt a Bayesian perspective and treat the unknown  $\tilde{\mathbf{H}}$  as a latent random variable. This allows us to recast the deterministic optimization problem (12) as a posterior inference problem over  $p(\mathbf{x}|\mathbf{Y}_p)$ , which is obtained by marginalizing over  $\tilde{\mathbf{H}}$ :

$$p(\mathbf{x}|\mathbf{Y}_p) = \int p(\mathbf{x}|\tilde{\mathbf{H}}) p(\tilde{\mathbf{H}}|\mathbf{Y}_p) d\tilde{\mathbf{H}}. \quad (13)$$

This integral involves two distributions. First, the *channel*

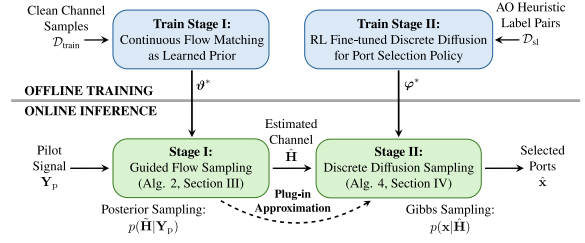


Fig. 2. Overall workflow of the proposed two-stage diffusion framework.

posterior  $p(\tilde{\mathbf{H}}|\mathbf{Y}_p) \propto p(\mathbf{Y}_p|\tilde{\mathbf{H}}) q(\tilde{\mathbf{H}})$  encapsulates the uncertainty over  $\tilde{\mathbf{H}}$  given the observations, where the likelihood  $p(\mathbf{Y}_p|\tilde{\mathbf{H}})$  is defined by the observation model in (3) and the prior factorizes as  $q(\tilde{\mathbf{H}}) = \prod_{k=1}^K q(\mathbf{h}_k)$  assuming spatial independence among geographically distributed users. Second, the *port selection distribution*  $p(\mathbf{x}|\tilde{\mathbf{H}})$  describes the probability of each port configuration given channel  $\tilde{\mathbf{H}}$ . Specifically, we define a Gibbs distribution

$$p(\mathbf{x}|\tilde{\mathbf{H}}) = \frac{1}{Z} \exp\left(\kappa \cdot U(\mathbf{x}, \tilde{\mathbf{H}})\right), \quad (14)$$

where  $U(\mathbf{x}, \tilde{\mathbf{H}}) = \min_k R_k(\mathbf{x}, \tilde{\mathbf{H}})$  is a utility function,  $\kappa > 0$  serves as the inverse temperature scale, and  $Z$  is a normalizing constant. Notably, in the limit  $\kappa \rightarrow \infty$ , the probability mass concentrates on the global optimum of the original optimization problem. As a result, the ultimate system objective under this probabilistic framework becomes a maximum-a-posteriori (MAP) estimation problem:

$$\mathbf{x}^* = \arg \max_{\mathbf{x} \in \mathcal{X}} p(\mathbf{x}|\mathbf{Y}_p), \quad (15)$$

where  $\mathcal{X} = \{\mathbf{x} \in \{0, 1\}^N : \|\mathbf{x}\|_1 = M\}$  represents the feasible set of all valid port selection strategies.

Directly solving the MAP problem in (15) still remains intractable due to the high-dimensional marginalization over the entire latent channel space. To bypass this, we apply a single-sample Monte Carlo (plug-in) approximation that decouples the original problem into two sequential sampling tasks:

$$\hat{\mathbf{H}} \sim p(\tilde{\mathbf{H}}|\mathbf{Y}_p), \quad \hat{\mathbf{x}} \sim p(\mathbf{x}|\hat{\mathbf{H}}), \quad (16)$$

which correspond to the channel estimation task (Stage I) and the port selection task (Stage II), respectively.

Specifically, this plug-in approximation corresponds to replacing the channel posterior with a Dirac delta function centered at a single posterior sample  $\hat{\mathbf{H}}$ , i.e.,  $p(\tilde{\mathbf{H}}|\mathbf{Y}_p) \approx \delta(\tilde{\mathbf{H}} - \hat{\mathbf{H}})$ . This collapses the intractable integration in (13) into a point evaluation, where  $\hat{\mathbf{H}}$  serves as a deterministic proxy for  $\tilde{\mathbf{H}}$ . The tightness of this approximation, which directly governs the severity of error propagation into Stage II, hinges on how sharply the channel posterior concentrates around its mode. To mitigate error propagation, we leverage flow-based diffusion models to learn a strong data-driven structural prior and perform high-fidelity approximate posterior sampling, as detailed in Section III.

In Stage II, conditioned on the estimated  $\hat{\mathbf{H}}$ , a port selection strategy  $\hat{\mathbf{x}}$  is drawn from the conditional distribution  $p(\mathbf{x}|\hat{\mathbf{H}})$ . Since the Gibbs distribution in (14) becomes sharply peaked around the global optimum as  $\kappa \rightarrow \infty$ , this sampling operation

is approximately equivalent to the exact MAP inference (i.e.,  $\hat{\mathbf{x}} \approx \mathbf{x}^*$ ). To achieve this conditional sampler, we employ a discrete diffusion model, the technical details of which are deferred to Section IV. The overall workflow of the proposed framework is illustrated in Fig. 2.

*Remark 1 (Unified MAP versus Heuristic Decoupling):* Although the resulting sequential execution resembles the conventional decoupled cascade, our two-stage framework serves as a principled approximation of the unified MAP objective in (15), which provides a rigorous mathematical justification for the sequential design.

### III. FLOW-BASED DIFFUSION FRAMEWORK FOR CHANNEL ESTIMATION

As illustrated in Section II-C, Stage I requires approximating and sampling from the channel posterior  $p(\tilde{\mathbf{H}}|\mathbf{Y}_p)$ . Hand-crafted priors, such as the angular-domain sparsity assumed in [16]–[18], fail to capture the intricate spatial correlations of FAS channels, making them inadequate to regularize the severely under-determined inverse problem in (3). To bridge this gap, we adopt a flow-based diffusion model to learn a powerful data-driven channel prior, whose generation process naturally accommodates measurement-guided approximate posterior sampling for channel estimation.

In this section, we first briefly outline the fundamentals of flow-based diffusion models, then introduce our offline prior learning strategy, and finally elaborate on the proposed online channel estimation framework via parallel guided generation.

#### A. Preliminaries on Flow-Based Diffusion Models

The fundamental objective of generative modeling is to learn a parameterized model  $p_\vartheta(\mathbf{h})$  that approximates a true data distribution  $q(\mathbf{h})$ , given a set of training samples  $\mathcal{D}_{\text{train}} = \{\mathbf{h}^{(i)}\}_{i=1}^{N_{\text{train}}}$  drawn from it<sup>2</sup>. Flow-based diffusion models achieve this by learning a continuous transformation from a standard Gaussian source distribution  $\mathcal{N}(0, \mathbf{I})$  to the target distribution  $q(\mathbf{h})$  via a continuous-time probability path  $\{p_t\}_{t \in [0,1]}$  [33]–[36], where  $t \in [0,1]$  parameterizes the evolution such that  $p_1 = \mathcal{N}(0, \mathbf{I})$  and  $p_0 = q$ .

Mathematically, this transformation is characterized by a time-dependent bijective mapping  $\psi_t$ , referred to as a *flow*, governed by an ordinary differential equation (ODE):

$$\frac{d\psi_t(\mathbf{z})}{dt} = \mathbf{v}_t(\psi_t(\mathbf{z})), \quad \text{with } \psi_1(\mathbf{z}) = \mathbf{z}, \quad (17)$$

where  $\mathbf{v}_t$  denotes the time-dependent velocity field. Physically,  $\mathbf{v}_t$  drives an initial noise sample  $\mathbf{z}_1 \sim \mathcal{N}(\mathbf{0}, \mathbf{I})$  along a continuous trajectory  $\mathbf{z}_t = \psi_t(\mathbf{z}_1)$  such that its marginal distribution precisely matches  $p_t$  throughout the evolution. Therefore, by solving the ODE from  $t = 1$  to  $t = 0$ , the flow deterministically maps  $\mathbf{z}_1$  into a structured channel realization  $\mathbf{h} = \mathbf{z}_0 = \psi_0(\mathbf{z}_1)$  that follows the target distribution.

To train this generative model, suppose we have defined a target marginal probability path  $p_t$  connecting the source distribution  $p_1 = p$  to the target data distribution  $p_0 = q$ , and let  $\mathbf{v}_t$  be its corresponding marginal velocity field. We can

then approximate  $\mathbf{v}_t$  using a neural network  $\mathbf{v}_t^\vartheta$  via the Flow Matching (FM) objective:

$$\mathcal{L}_{\text{FM}}(\vartheta) = \mathbb{E}_{t, \mathbf{z}_t \sim p_t} \left[ \|\mathbf{v}_t(\mathbf{z}_t) - \mathbf{v}_t^\vartheta(\mathbf{z}_t)\|_2^2 \right]. \quad (18)$$

Despite being conceptually straightforward, this objective is intractable to evaluate in practice. Specifically, as suggested by [34], a feasible way to construct  $p_t$  is through marginalization over simpler conditional probability paths  $p_t(\mathbf{z}_t|\mathbf{h})$ :

$$p_t(\mathbf{z}_t) = \int p_t(\mathbf{z}_t|\mathbf{h})q(\mathbf{h})d\mathbf{h}. \quad (19)$$

As a result, the corresponding marginal velocity field  $\mathbf{v}_t$  can be expressed as the posterior expectation of the conditional velocity fields:

$$\begin{aligned} \mathbf{v}_t(\mathbf{z}_t) &= \mathbb{E}_{\mathbf{h} \sim p_t(\cdot|\mathbf{z}_t)}[\mathbf{v}_t(\mathbf{z}_t|\mathbf{h})] \\ &= \int \mathbf{v}_t(\mathbf{z}_t|\mathbf{h}) \frac{p_t(\mathbf{z}_t|\mathbf{h})q(\mathbf{h})}{p_t(\mathbf{z}_t)} d\mathbf{h}, \end{aligned} \quad (20)$$

where  $\mathbf{v}_t(\mathbf{z}_t|\mathbf{h})$  denotes the conditional velocity field that generates  $p_t(\mathbf{z}_t|\mathbf{h})$ . Evidently, computing this expectation requires intractable integration over the entire unknown data distribution  $q(\mathbf{h})$ .

To bypass this computational bottleneck, an alternative Conditional Flow Matching (CFM) objective was proposed in [34], which directly regresses the neural network against the conditional velocity field:

$$\mathcal{L}_{\text{CFM}}(\vartheta) = \mathbb{E}_{t, \mathbf{h} \sim q, \mathbf{z}_t \sim p_t(\cdot|\mathbf{h})} \left[ \|\mathbf{v}_t(\mathbf{z}_t|\mathbf{h}) - \mathbf{v}_t^\vartheta(\mathbf{z}_t)\|_2^2 \right], \quad (21)$$

and it has been proven that optimizing this CFM objective is mathematically equivalent to the original FM objective, since they share the same gradient with respect to  $\vartheta$ .

Once the network  $\mathbf{v}_t^\vartheta$  is trained, generation is realized by drawing  $\mathbf{z}_1 \sim \mathcal{N}(0, \mathbf{I})$  and then numerically solving the flow ODE from  $t = 1$  to  $t = 0$  using solvers like the Euler method:

$$\mathbf{z}_{t-\Delta t} = \mathbf{z}_t - \mathbf{v}_t(\mathbf{z}_t)\Delta t, \quad (22)$$

where  $\Delta t$  is the discretization step size. By adjusting the number of function evaluations (NFEs), one can flexibly trade off sample generation quality against inference speed.

#### B. Offline Training: Learning the Flow-Based Channel Prior

To instantiate the CFM objective defined in (21) for model training, we must design a specific conditional probability path  $p_t(\mathbf{z}_t|\mathbf{h})$  and its corresponding conditional velocity field  $\mathbf{v}_t(\mathbf{z}_t|\mathbf{h})$ .

##### 1) Affine Conditional Flow and Optimal Transport

For mathematical simplicity, we consider the affine conditional flow, where the intermediate state  $\mathbf{z}_t$  is explicitly constructed by linearly interpolating between a data sample  $\mathbf{h} \sim q$  and a specific noise sample  $\mathbf{z}_1 \sim \mathcal{N}(0, \mathbf{I})$ :

$$\mathbf{z}_t = \psi_t(\mathbf{z}_1|\mathbf{h}) = a_t\mathbf{h} + b_t\mathbf{z}_1. \quad (23)$$

To fulfill the required boundary conditions (i.e.,  $p_0 = q$  and  $p_1 = p$ ), the time-dependent coefficients must satisfy  $a_0 = 1, b_0 = 0$  at  $t = 0$ , and  $a_1 = 0, b_1 = 1$  at  $t = 1$ . While any coefficient schedule satisfying these boundary conditions is theoretically valid, we adopt the Optimal Transport (OT) formulation by setting  $a_t = 1 - t$  and  $b_t = t$ , i.e.,

$$\mathbf{z}_t = (1 - t)\mathbf{h} + t\mathbf{z}_1. \quad (24)$$

<sup>2</sup>We omit the user index  $k$  for notational simplicity and use  $\mathbf{h}$  to denote the real-equivalent channel vector of an individual user, defined in (4).

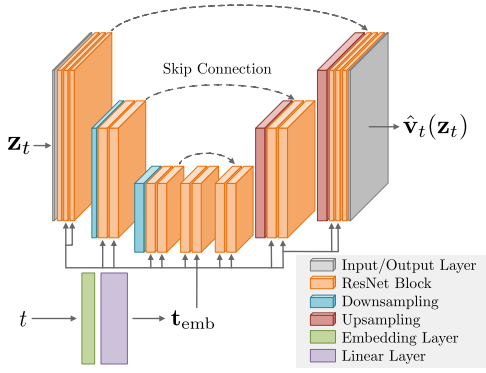


Fig. 3. An illustration of the velocity network  $\mathbf{v}_t^\vartheta$ , implemented using a lightweight U-Net architecture with sinusoidal time embedding.

This OT path forms a straight-line trajectory between any noise-data pair, which minimizes the discretization error of numerical ODE solvers at larger generation step sizes.

Taking the time derivative of (23), the conditional velocity field  $\mathbf{v}_t(\mathbf{z}_t|\mathbf{h})$  under the OT path admits a closed form

$$\mathbf{v}_t(\mathbf{z}_t|\mathbf{h}) = \frac{da_t}{dt}\mathbf{h} + \frac{db_t}{dt}\mathbf{z}_1 = \mathbf{z}_1 - \mathbf{h}. \quad (25)$$

Furthermore, since the randomness of  $\mathbf{z}_t$  conditioned on  $\mathbf{h}$  originates entirely from the initial noise  $\mathbf{z}_1$ , we can apply the reparameterization trick to replace the expectation over  $\mathbf{z}_t \sim p_t(\cdot|\mathbf{h})$  with an expectation over the noise source  $\mathbf{z}_1 \sim p$ . Thus, the CFM objective for our flow-based model reduces to:

$$\mathcal{L}_{\text{CFM}}(\vartheta) = \mathbb{E}_{t, \mathbf{h} \sim q, \mathbf{z}_1 \sim p} \left[ \|\mathbf{v}_t^\vartheta(\mathbf{z}_t) - (\mathbf{z}_1 - \mathbf{h})\|_2^2 \right]. \quad (26)$$

This objective is highly tractable, requiring only available training samples, standard Gaussian noise, and basic algebraic operations, thereby completely bypassing any complicated numerical integration.

### 2) Network Architecture and Offline Training

Similar to our previous SISO-FAS work [39], we adopt a lightweight U-Net as the backbone of the velocity network  $\mathbf{v}_t^\vartheta$  to predict  $\hat{\mathbf{v}}_t(\mathbf{z}_t)$ . As illustrated in Fig. 3, the network employs a symmetric encoder-decoder topology with three resolution levels, utilizing ResNet blocks for feature extraction and skip connections to preserve fine-grained spatial features. To explicitly exploit the local spatial correlation inherent in 2D FAS channels, the 1D latent variable  $\mathbf{z}_t \in \mathbb{R}^{2N \times 1}$  is reshaped into a  $2 \times N_x \times N_y$  spatial tensor, where the two channels correspond to the real and imaginary components. Furthermore, to ensure the network is time-aware, the continuous time variable  $t \in [0, 1]$  is encoded via a sinusoidal positional embedding  $\mathbf{t}_{\text{emb}} \in \mathbb{R}^{D_{\text{emb}}}$  and injected into every ResNet block.

We train  $\mathbf{v}_t^\vartheta$  by minimizing the OT-based CFM objective in (26) via mini-batch stochastic gradient descent (SGD). At each iteration, given a mini-batch of  $B$  samples drawn from the offline dataset  $\mathcal{D}_{\text{train}} = \{\mathbf{h}^{(i)}\}_{i=1}^{N_{\text{train}}}$ , we independently sample continuous time steps  $t^{(i)} \sim \mathcal{U}[0, 1]$  and source noise  $\mathbf{z}_1^{(i)} \sim \mathcal{N}(\mathbf{0}, \mathbf{I})$ . Following the OT conditional flow formulation, the intermediate state is constructed as  $\mathbf{z}_{t^{(i)}}^{(i)} = (1 - t^{(i)})\mathbf{h}^{(i)} + t^{(i)}\mathbf{z}_1^{(i)}$ . Consequently, the neural network parameters  $\vartheta$  are updated using the gradient of the following empirical loss:

$$\hat{\mathcal{L}}_{\text{CFM}}(\vartheta) = \frac{1}{B} \sum_{i=1}^B \left\| \mathbf{v}_{t^{(i)}}^\vartheta(\mathbf{z}_{t^{(i)}}^{(i)}) - (\mathbf{z}_1^{(i)} - \mathbf{h}^{(i)}) \right\|_2^2. \quad (27)$$

### Algorithm 1 Offline Flow-Based Diffusion Model Training

**Require:** Training dataset  $\mathcal{D}_{\text{train}} = \{\mathbf{h}^{(i)}\}_{i=1}^{N_{\text{train}}}$ , batch size  $B$ , learning rate  $\zeta$ .

- 1: **repeat**
- 2:   **for**  $i = 1$  **to**  $B$  **do**
- 3:     Sample  $\mathbf{h}^{(i)}$  from  $\mathcal{D}_{\text{train}}$
- 4:     Sample  $t^{(i)} \sim \mathcal{U}[0, 1]$
- 5:     Sample  $\mathbf{z}_1^{(i)} \sim \mathcal{N}(\mathbf{0}, \mathbf{I})$
- 6:     Construct  $\mathbf{z}_{t^{(i)}}^{(i)} = (1 - t^{(i)})\mathbf{h}^{(i)} + t^{(i)}\mathbf{z}_1^{(i)}$
- 7:   **end for**
- 8:   Compute  $\hat{\mathcal{L}}_{\text{CFM}}$  according to Eq. (27)
- 9:   Update  $\vartheta \leftarrow \vartheta - \zeta \nabla_{\vartheta} \hat{\mathcal{L}}_{\text{CFM}}$  via SGD/Adam
- 10: **until** convergence

The overall training procedure is summarized in Algorithm 1.

### C. Online Inference: Simultaneous Multiuser Channel Estimation via Measurement-Consistent Flow Guidance

When deploying the offline-trained velocity network  $\mathbf{v}_t^\vartheta$  for online multiuser channel estimation, directly solving the flow ODEs from  $K$  independent Gaussian initializations  $\mathbf{z}_{k,1} \sim \mathcal{N}(\mathbf{0}, \mathbf{I})$  would yield unconditional random samples that ignore the pilot observations in (3). To enforce measurement consistency during inference, the generative trajectories must be guided to align with the received signals. To this end, we draw inspiration from the FlowDPS [37] framework to design a unified measurement consistency scheme that facilitates parallel guided generation across all users, as detailed below.

#### 1) Flow Decomposition

To effectively guide the generation process, it is necessary to isolate the model's instantaneous estimate of the clean channel at any intermediate state. As the generation process is governed by the numerical integration of the flow ODE in (22), we proceed by decomposing its two core components: the velocity field  $\mathbf{v}_t$  and the intermediate state  $\mathbf{z}_t$ . For brevity, the user index  $k$  is omitted in the following derivations.

First, according to (20), the instantaneous marginal velocity at a specific intermediate state  $\mathbf{z}_t$  is essentially the posterior expectation of the conditional velocities across all trajectories passing through  $\mathbf{z}_t$ . By substituting the OT conditional velocity (25) into (20) and leveraging the linearity of expectation,  $\mathbf{v}_t(\mathbf{z}_t)$  can be analytically decomposed as

$$\begin{aligned} \mathbf{v}_t(\mathbf{z}_t) &= \mathbb{E}[\mathbf{v}_t(\mathbf{z}_t|\mathbf{h})|\mathbf{z}_t] \\ &= \mathbb{E}[\mathbf{z}_1 - \mathbf{h}|\mathbf{z}_t] = \hat{\mathbf{z}}_{1|t} - \hat{\mathbf{h}}_{0|t}, \end{aligned} \quad (28)$$

where  $\hat{\mathbf{h}}_{0|t} = \mathbb{E}[\mathbf{h}|\mathbf{z}_t]$  and  $\hat{\mathbf{z}}_{1|t} = \mathbb{E}[\mathbf{z}_1|\mathbf{z}_t]$  denote the MMSE estimates of the clean channel and the corresponding source noise, respectively, given  $\mathbf{z}_t$ . Similarly,  $\mathbf{z}_t$  itself can be decomposed as a weighted average of these two estimates<sup>3</sup>:

$$\begin{aligned} \mathbf{z}_t &= \mathbb{E}[\mathbf{z}_t|\mathbf{z}_t] \\ &= \mathbb{E}[(1 - t)\mathbf{h} + t\mathbf{z}_1|\mathbf{z}_t] = (1 - t)\hat{\mathbf{h}}_{0|t} + t\hat{\mathbf{z}}_{1|t}. \end{aligned} \quad (29)$$

By rearranging (28) and (29) to isolate the two MMSE estimates, and replacing the exact marginal velocity with our

<sup>3</sup>With a slight abuse of notation in  $\mathbb{E}[\mathbf{z}_t|\mathbf{z}_t]$ , the  $\mathbf{z}_t$  in the conditioning represents a specific deterministic realization, while the other  $\mathbf{z}_t$  denotes the random variable itself.

neural approximation  $\mathbf{v}_t^\vartheta(\mathbf{z}_t) \approx \mathbf{v}_t(\mathbf{z}_t)$ , we obtain the flow-based version of Tweedie’s formula under the OT path [37]:

$$\hat{\mathbf{h}}_{0|t} = \mathbf{z}_t - t\mathbf{v}_t^\vartheta(\mathbf{z}_t), \quad (30)$$

$$\hat{\mathbf{z}}_{1|t} = \mathbf{z}_t + (1-t)\mathbf{v}_t^\vartheta(\mathbf{z}_t), \quad (31)$$

which provides a tractable way to “peek” at the clean sample  $\hat{\mathbf{h}}_{0|t}$  and the source noise  $\hat{\mathbf{z}}_{1|t}$  from any  $\mathbf{z}_t$  during generation.

Finally, by substituting the decompositions (29) and (28) back into the standard Euler update step (22), the transition to the next intermediate state  $\mathbf{z}_{t-\Delta t}$  can be reformulated as:

$$\begin{aligned} \mathbf{z}_{t-\Delta t} &= \mathbf{z}_t - \mathbf{v}_t^\vartheta(\mathbf{z}_t)\Delta t \\ &= \left[ (1-t)\hat{\mathbf{h}}_{0|t} + t\hat{\mathbf{z}}_{1|t} \right] - \left[ \hat{\mathbf{z}}_{1|t} - \hat{\mathbf{h}}_{0|t} \right] \Delta t \\ &= (1-(t-\Delta t))\hat{\mathbf{h}}_{0|t} + (t-\Delta t)\hat{\mathbf{z}}_{1|t}. \end{aligned} \quad (32)$$

Notably, this decomposed update explicitly reveals that  $\mathbf{z}_{t-\Delta t}$  retains the same weighted-combination structure as  $\mathbf{z}_t$ , with the time coefficients simply updated to  $1-(t-\Delta t)$  and  $t-\Delta t$ . This decoupled formulation provides a natural and tractable anchor to enforce measurement consistency on  $\hat{\mathbf{h}}_{0|t}$  at each integration step, as detailed in the subsequent discussion.

### 2) Unified Guidance on $\hat{\mathbf{h}}_{0|t}$

We now re-introduce the user index  $k$  to elaborate on the unified measurement consistency guidance procedure. Specifically, we let  $\hat{\mathbf{h}}_{k,0|t}$  represent the predicted clean channel estimate for every user  $k \in \{1, \dots, K\}$  from the intermediate states  $\mathbf{z}_{k,t}$  at time step  $t$ . Analogous to (6), the corresponding prediction of the complete multiuser channel matrix  $\hat{\mathbf{H}}_{0|t}$  can be assembled as:

$$\hat{\mathbf{H}}_{0|t} = [f^{-1}(\hat{\mathbf{h}}_{1,0|t}), f^{-1}(\hat{\mathbf{h}}_{2,0|t}), \dots, f^{-1}(\hat{\mathbf{h}}_{K,0|t})]. \quad (33)$$

Following the signal model described in (3), we define the measurement consistency loss  $\mathcal{L}_{\text{MC}}$  to penalize the discrepancy between the actual received pilot matrix  $\mathbf{Y}_p$  and the reconstructed pilot observations derived from our current clean prediction  $\hat{\mathbf{H}}_{0|t}$ :

$$\mathcal{L}_{\text{MC}} = \frac{1}{2} \left\| \mathbf{Y}_p - \Omega_{\mathcal{O}} \hat{\mathbf{H}}_{0|t} \mathbf{P} \right\|_F^2. \quad (34)$$

To steer the generative trajectories toward a solution that satisfies the actual pilot observation, we directly perform gradient descent on the predicted clean channel estimates by moving along the negative gradient of the measurement consistency loss:

$$\hat{\mathbf{H}}_{0|t}(\mathbf{Y}_p) = \hat{\mathbf{H}}_{0|t} - \alpha_t \nabla_{\hat{\mathbf{H}}_{0|t}} \mathcal{L}_{\text{MC}}, \quad (35)$$

where  $\alpha_t$  is a time-dependent step size and the gradient has a closed-form expression given by

$$\nabla_{\hat{\mathbf{H}}_{0|t}} \mathcal{L}_{\text{MC}} = -\Omega_{\mathcal{O}}^H \left( \mathbf{Y}_p - \Omega_{\mathcal{O}} \hat{\mathbf{H}}_{0|t} \mathbf{P} \right) \mathbf{P}^H. \quad (36)$$

Finally, by extracting the  $k$ -th column of the updated matrix  $\hat{\mathbf{H}}_{0|t}(\mathbf{Y}_p)$  (denoted by  $[\cdot]_{:,k}$ ) and applying the forward isomorphic mapping  $f$ , the observation-guided clean channel estimate for each individual user at time step  $t$  is given by

$$\hat{\mathbf{h}}_{k,0|t}(\mathbf{Y}_p) = f \left( \left[ \hat{\mathbf{H}}_{0|t}(\mathbf{Y}_p) \right]_{:,k} \right). \quad (37)$$

### 3) Practical Techniques for Robust Guidance

Although (35) provides a straightforward mechanism for measurement consistency guidance, a stable and robust im-

plementation requires three practical techniques:

- **Gradient Normalization:** The magnitude of  $\nabla_{\hat{\mathbf{H}}_{0|t}} \mathcal{L}_{\text{MC}}$  is extremely volatile in the early generation stages (i.e.,  $t \rightarrow 1$ ), where the model’s prediction is highly uncertain and incurs massive discrepancies with  $\mathbf{Y}_p$ . We resolve this by normalizing the gradient by its Frobenius norm, so that each update magnitude is purely controlled by  $\alpha_t$ :

$$\hat{\mathbf{H}}_{0|t}(\mathbf{Y}_p) = \hat{\mathbf{H}}_{0|t} - \alpha_t \frac{\nabla_{\hat{\mathbf{H}}_{0|t}} \mathcal{L}_{\text{MC}}}{\|\nabla_{\hat{\mathbf{H}}_{0|t}} \mathcal{L}_{\text{MC}}\|_F}. \quad (38)$$

- **Multi-Step Optimization and Interpolation:** A single gradient step per numerical integration step is typically insufficient to pull the trajectories into the desired measurement subspace. Inspired by Decomposed Diffusion Sampling (DDS) [40], we execute  $N_{\text{iter}}$  consecutive gradient steps (e.g.,  $N_{\text{iter}} = 3$ ). To mitigate over-correction while maintaining alignment with the learned channel prior, we interpolate the guided result with the unguided estimate  $\hat{\mathbf{H}}_{0|t}$  to form the final combined sample:

$$\hat{\mathbf{H}}_{0|t}^{\text{guided}} = (1-\gamma_t)\hat{\mathbf{H}}_{0|t} + \gamma_t\hat{\mathbf{H}}_{0|t}(\mathbf{Y}_p). \quad (39)$$

We set  $\gamma_t = t$ , so that measurement consistency dominates early while the learned prior takes over as  $t \rightarrow 0$ .

- **Injection of Stochasticity:** Since  $\mathbf{Y}_p$  is corrupted by AWGN, simply minimizing  $\mathcal{L}_{\text{MC}}$  would cause the generation trajectories to overfit this noise. To prevent this, we inject stochasticity into the latent source noise estimate  $\hat{\mathbf{z}}_{k,1|t}$  prior to the Euler numerical integration step:

$$\hat{\mathbf{z}}_{k,1|t}^{\text{stoch}} = \sqrt{1-\eta_t}\hat{\mathbf{z}}_{k,1|t} + \sqrt{\eta_t}\epsilon, \quad (40)$$

where  $\epsilon \sim \mathcal{N}(0, \mathbf{I})$ . The variance schedule  $\eta_t = 1 - (t - \Delta t)$  increases as  $t \rightarrow 0$ , acting as a progressively stronger regularizer against noise overfitting. This injected stochasticity preserves the final estimation accuracy, because the Euler update (32) weights the noise term by  $t - \Delta t$ , which vanishes as  $t \rightarrow 0$ .

The overall algorithm of the parallel measurement consistency guided generation for multiuser channel estimation is summarized in Algorithm 2.

*Remark 2 (Bayesian Interpretation):* The measurement consistency-guided generation in Algorithm 2 admits a formal Bayesian interpretation as approximate posterior sampling from  $p_{\vartheta}(\tilde{\mathbf{H}}|\mathbf{Y}_p) \propto p(\mathbf{Y}_p|\tilde{\mathbf{H}})p_{\vartheta}(\tilde{\mathbf{H}})$ , where the joint prior factorizes as  $p_{\vartheta}(\tilde{\mathbf{H}}) = \prod_{k=1}^K p_{\vartheta}(\mathbf{h}_k)$  under the user independence assumption established in Section II, and the measurement consistency gradient  $\nabla_{\hat{\mathbf{H}}_{0|t}} \mathcal{L}_{\text{MC}}$  corresponds to the likelihood score of the observation model in (3). This relationship formally aligns our Stage I with the probabilistic framework introduced in Section II-C. For rigorous mathematical justification regarding this approximation, we refer interested readers to [37].

### D. Complexity Analysis

We now characterize the asymptotic computational complexity of the proposed online channel estimator summarized in Algorithm 2. The overall computational cost is dominated by the U-Net forward passes and the measurement consistency gradient evaluations. Accordingly, we first quantify

---

**Algorithm 2** Online Flow-Based Channel Estimation
 

---

**Require:** Pilot observation  $\mathbf{Y}_p$ , offline-trained velocity network  $\mathbf{v}_t^\vartheta$ , user count  $K$ , integration step size  $\Delta t$ , optimization steps  $N_{\text{iter}}$ , gradient step size  $\alpha_t$ .

- 1: **Initialize:**  $\mathbf{z}_{k,1} \sim \mathcal{N}(\mathbf{0}, \mathbf{I})$  for  $k = 1, \dots, K$
- 2: **for**  $t = 1$  **down to** 0 **with step size**  $\Delta t$  **do**
- 3:   *% 1. Flow Decomposition for Parallel Trajectories*
- 4:   **for**  $k = 1$  **to**  $K$  **do**
- 5:     Compute  $\hat{\mathbf{h}}_{k,0|t} = \mathbf{z}_{k,t} - t\mathbf{v}_t^\vartheta(\mathbf{z}_{k,t})$
- 6:     Compute  $\hat{\mathbf{z}}_{k,1|t} = \mathbf{z}_{k,t} + (1-t)\mathbf{v}_t^\vartheta(\mathbf{z}_{k,t})$
- 7:   **end for**
- 8:   *% 2. Matrix Assembly for Unified Guidance*
- 9:   Construct multiuser matrix  $\hat{\mathbf{H}}_{0|t}$  via (33)
- 10:   Initialize guided estimate  $\hat{\mathbf{H}}_{0|t}(\mathbf{Y}_p) = \hat{\mathbf{H}}_{0|t}$
- 11:   *% 3. Normalized Multi-Step Guidance*
- 12:   **for**  $i = 1$  **to**  $N_{\text{iter}}$  **do**
- 13:     Evaluate gradient  $\nabla \mathcal{L}_{\text{MC}}$  via (36) at  $\hat{\mathbf{H}}_{0|t}(\mathbf{Y}_p)$
- 14:     Update  $\hat{\mathbf{H}}_{0|t}(\mathbf{Y}_p) \leftarrow \hat{\mathbf{H}}_{0|t}(\mathbf{Y}_p) - \alpha_t \frac{\nabla \mathcal{L}_{\text{MC}}}{\|\nabla \mathcal{L}_{\text{MC}}\|_F}$
- 15:   **end for**
- 16:   *% 4. Interpolation to Preserve Structural Prior*
- 17:   Compute  $\hat{\mathbf{H}}_{0|t}^{\text{guided}} = (1-\gamma_t)\hat{\mathbf{H}}_{0|t} + \gamma_t\hat{\mathbf{H}}_{0|t}(\mathbf{Y}_p)$
- 18:   *% 5. Trajectory Update via Euler Step*
- 19:   Let  $t' = t - \Delta t$
- 20:   **for**  $k = 1$  **to**  $K$  **do**
- 21:     Extract  $\hat{\mathbf{h}}_{k,0|t}^{\text{guided}} = f\left(\left[\hat{\mathbf{H}}_{0|t}^{\text{guided}}\right]_{:,k}\right)$
- 22:     Inject noise stochasticity via (40)
- 23:     Compute Euler update  $\mathbf{z}_{k,t'} = (1-t')\hat{\mathbf{h}}_{k,0|t}^{\text{guided}} + t'\hat{\mathbf{z}}_{k,1|t}^{\text{stoch}}$
- 24:   **end for**
- 25: **end for**
- 26: **Output:** Estimated channels  $\hat{\mathbf{h}}_k = \mathbf{z}_{k,0}, \forall k = 1, \dots, K$

---

the complexity of a single U-Net forward pass. A standard convolutional layer operating on a spatial tensor of  $N$  pixels with  $C$  channels using  $F \times F$  kernels requires approximately  $2NC^2F^2$  Floating-Point Operations (FLOPs). Treating the kernel size as a constant (i.e.,  $F = 3$  in our implementation), the per-layer complexity simplifies to  $\mathcal{O}(NC^2)$ . Since our U-Net has a constant number of layers, the overall forward pass complexity is bounded by  $\mathcal{O}(NC_{\text{max}}^2)$ , where  $C_{\text{max}}$  denotes the maximum channel count across all layers.

In each iteration, the algorithm performs  $K$  parallel U-Net forward passes to compute the flow decomposition for each user (lines 4–7), followed by  $N_{\text{iter}}$  multi-step measurement consistency gradient updates on the assembled multiuser estimate (lines 12–15). The gradient computation in (36) is dominated by the matrix multiplication with the orthogonal pilot codebook  $\mathbf{P}$ , since the selection operator  $\Omega_{\mathcal{O}}$  is binary and incurs no floating-point cost. Each gradient evaluation therefore costs  $\mathcal{O}(N_{\mathcal{O}}K^2)$ . Finally, the total number of iterations is given by  $\text{NFE} \triangleq 1/\Delta t$ . Aggregating over all iterations and using the relation  $N_{\mathcal{O}} = \delta N$ , where  $\delta$  is the sub-sampling ratio, the total complexity of the proposed channel estimator is given by  $\mathcal{O}(\text{NFE} \cdot N \cdot [KC_{\text{max}}^2 + N_{\text{iter}} \cdot \delta K^2])$ .

#### IV. DISCRETE DIFFUSION-BASED PORT SELECTION

With the individual channel vectors  $\hat{\mathbf{h}}_k$  obtained via Algorithm 2, we assemble the estimated multiuser channel matrix

as  $\hat{\mathbf{H}} = [f^{-1}(\hat{\mathbf{h}}_1), \dots, f^{-1}(\hat{\mathbf{h}}_K)]$ , which deterministically replaces the latent  $\tilde{\mathbf{H}}$  under the plug-in approximation in (16). The task of Stage II is then to approximate the conditional port selection distribution  $p(\mathbf{x}|\tilde{\mathbf{H}})$  defined in (14) and draw a selection strategy given  $\hat{\mathbf{H}}$ . To achieve this, we employ a discrete diffusion model to learn a parametric approximation  $p_\varphi(\mathbf{x}|\hat{\mathbf{H}})$  to this target distribution. Since the Gibbs distribution concentrates probability mass on port configurations with high utility  $U(\mathbf{x}, \hat{\mathbf{H}}) = \min_k R_k(\mathbf{x}, \hat{\mathbf{H}})$ , training  $p_\varphi$  to approximate this target translates into optimizing the model to maximize the expected utility:

$$\arg \max_{\varphi} \mathbb{E}_{\tilde{\mathbf{H}} \sim p(\tilde{\mathbf{H}}), \mathbf{x} \sim p_\varphi(\mathbf{x}|\tilde{\mathbf{H}})} [U(\mathbf{x}, \tilde{\mathbf{H}})]. \quad (41)$$

In this section, we first briefly introduce the fundamentals of discrete diffusion models. We then elaborate on a supervised learning-based training strategy designed to fit the port selection posterior, and finally present a reinforcement fine-tuning procedure that enables the learned sampler to surpass the supervised baseline.

##### A. Preliminaries on Discrete Diffusion Models

Since our objective is to generate a binary mask  $\mathbf{x} \in \{0, 1\}^N$ , the continuous flow-based diffusion framework introduced in Section III-A is no longer applicable. Instead, we adopt a discrete diffusion modeling framework [41]. Let  $q(\mathbf{x})$  denote the target discrete distribution. Aligned with the standard denoising diffusion probability models (DDPM) [42], the generative process is formulated as a  $T$ -step Markov chain:

$$p_\varphi(\mathbf{x}_{0:T}) = p(\mathbf{x}_T) \prod_{t=1}^T p_\varphi(\mathbf{x}_{t-1}|\mathbf{x}_t), \quad (42)$$

where the intermediate states  $\mathbf{x}_{1:T}$  share the same dimensionality as the original data  $\mathbf{x}_0$ . The learned distribution  $p_\varphi$  is then recovered by marginalizing over the discrete intermediate states:  $p_\varphi(\mathbf{x}_0) = \sum_{\mathbf{x}_{1:T}} p_\varphi(\mathbf{x}_{0:T})$ .

This generative process aims to reverse a fixed forward diffusion that progressively corrupts data into noise. By converting the binary state  $\mathbf{x}$  into a one-hot categorical representation  $\tilde{\mathbf{x}} = [\mathbf{1} - \mathbf{x} \quad \mathbf{x}] \in \{0, 1\}^{N \times 2}$  (where  $\mathbf{1}$  is the all-ones vector), the forward transition is specified as

$$q(\mathbf{x}_t|\mathbf{x}_{t-1}) = \text{Cat}(\mathbf{x}_t; \mathbf{p} = \tilde{\mathbf{x}}_{t-1} \mathbf{Q}_t), \quad (43)$$

where  $\text{Cat}(\cdot)$  denotes the categorical distribution, and  $\mathbf{Q}_t \in \mathbb{R}^{2 \times 2}$  is the transition probability matrix given by

$$\mathbf{Q}_t = \begin{bmatrix} 1 - \beta_t & \beta_t \\ \beta_t & 1 - \beta_t \end{bmatrix}. \quad (44)$$

Here, the predefined noise schedule  $\beta_t \in (0, 1)$  is designed such that  $\prod_{t=1}^T (1 - \beta_t) \approx 0$ , ensuring the final state  $\mathbf{x}_T$  converges to a uniform distribution. Leveraging the Markov property, the  $t$ -step marginal conditioned on  $\mathbf{x}_0$  admits a closed form:  $q(\mathbf{x}_t|\mathbf{x}_0) = \text{Cat}(\mathbf{x}_t; \mathbf{p} = \tilde{\mathbf{x}}_0 \mathbf{Q}_t)$ , where  $\mathbf{Q}_t = \prod_{i=1}^t \mathbf{Q}_i$  is the cumulative transition matrix.

To parameterize the reverse process in (42), a neural network is trained to predict the clean data distribution  $p_\varphi(\hat{\mathbf{x}}_0|\mathbf{x}_t)$ . The reverse transition is then recovered by marginalizing over all possible predicted states:

$$p_\varphi(\mathbf{x}_{t-1}|\mathbf{x}_t) = \sum_{\hat{\mathbf{x}}_0} q(\mathbf{x}_{t-1}|\mathbf{x}_t, \hat{\mathbf{x}}_0) p_\varphi(\hat{\mathbf{x}}_0|\mathbf{x}_t). \quad (45)$$

Here, the exact posterior  $q(\mathbf{x}_{t-1}|\mathbf{x}_t, \mathbf{x}_0)$  can be computed in closed form via Bayes' rule:

$$\begin{aligned} q(\mathbf{x}_{t-1}|\mathbf{x}_t, \mathbf{x}_0) &= \frac{q(\mathbf{x}_t|\mathbf{x}_{t-1}, \mathbf{x}_0)q(\mathbf{x}_{t-1}|\mathbf{x}_0)}{q(\mathbf{x}_t|\mathbf{x}_0)} \\ &= \text{Cat}\left(\mathbf{x}_{t-1}; \mathbf{p} = \frac{\tilde{\mathbf{x}}_t \mathbf{Q}_t^\top \odot \tilde{\mathbf{x}}_0 \bar{\mathbf{Q}}_{t-1}}{\tilde{\mathbf{x}}_0 \mathbf{Q}_t \tilde{\mathbf{x}}_t^\top}\right), \end{aligned} \quad (46)$$

where  $\odot$  denotes the element-wise Hadamard product.

The network parameters  $\varphi$  are optimized by minimizing the negative evidence lower bound (ELBO), which decomposes into three components:

$$\begin{aligned} \mathcal{L}_{\text{VB}}(\varphi) &= \mathbb{E}_q \left[ \sum_{t=2}^T \underbrace{D_{\text{KL}}(q(\mathbf{x}_{t-1}|\mathbf{x}_t, \mathbf{x}_0) \| p_\varphi(\mathbf{x}_{t-1}|\mathbf{x}_t))}_{\mathcal{L}_{t-1}} \right. \\ &\quad \left. - \underbrace{\log p_\varphi(\mathbf{x}_0|\mathbf{x}_1)}_{\mathcal{L}_0} + \underbrace{D_{\text{KL}}(q(\mathbf{x}_T|\mathbf{x}_0) \| p(\mathbf{x}_T))}_{\mathcal{L}_T} \right], \end{aligned} \quad (47)$$

where the expectation is taken over the joint forward trajectory  $q(\mathbf{x}_{0:T}) = q(\mathbf{x}_0) \prod_{t=1}^T q(\mathbf{x}_t|\mathbf{x}_{t-1})$ . The prior matching term  $\mathcal{L}_T$  is constant with respect to  $\varphi$  and is thus ignored. More importantly, for binary random variables, both  $\mathcal{L}_0$  and  $\mathcal{L}_{t-1}$  reduce to the expected cross-entropy between the predicted probability distribution  $p_\varphi(\hat{\mathbf{x}}_0|\mathbf{x}_t)$  and the one-hot representation  $\tilde{\mathbf{x}}_0$ , which effectively serves as a deterministic ground-truth distribution. Intuitively, since (45) constructs  $p_\varphi(\mathbf{x}_{t-1}|\mathbf{x}_t)$  by marginalizing the exact posterior  $q(\mathbf{x}_{t-1}|\mathbf{x}_t, \mathbf{x}_0)$  over the predicted state  $\hat{\mathbf{x}}_0$ , matching them via  $\mathcal{L}_{t-1}$  thus reduces to accurately predicting the ground truth  $\tilde{\mathbf{x}}_0$ . As a result, for a specific target data  $\mathbf{x}_0$ , the model can be tractably optimized via a surrogate binary cross-entropy (BCE) loss:

$$\mathcal{L}_{\text{BCE}}(\varphi, \mathbf{x}_0) = \mathbb{E}_{t, \mathbf{x}_t} \left[ - \sum_{n=1}^N \log p_\varphi(\hat{x}_{0,n} = x_{0,n}|\mathbf{x}_t) \right]. \quad (48)$$

The overall objective is then to minimize  $\mathbb{E}_{\mathbf{x}_0 \sim q}[\mathcal{L}_{\text{BCE}}(\varphi, \mathbf{x}_0)]$ , which can be easily optimized via SGD in model training.

### B. Supervised Learned Solver for Port Selection

While the general discrete diffusion framework introduced above aims to fit an unconditional target distribution  $q$ , our goal in Stage II is to learn a conditional distribution  $p_\varphi(\mathbf{x}|\tilde{\mathbf{H}})$  to maximize the expected utility in (41). Analogous to the unconditional case in (45), learning this conditional distribution relies on a neural network to predict the clean data distribution  $p_\varphi(\hat{\mathbf{x}}_0|\mathbf{x}_t, \tilde{\mathbf{H}})$  from any intermediate mask  $\mathbf{x}_t$ . To parameterize this conditional prediction, we utilize the same lightweight U-Net detailed in Section III-B2, with a slight modification in the input layer. Specifically, the  $K$  real-equivalent channel vectors  $\{\mathbf{h}_k\}_{k=1}^K$  and the current mask  $\mathbf{x}_t$  are reshaped and concatenated into a single  $(2K+1) \times N_x \times N_y$  spatial tensor for joint processing. However, since our goal is utility maximization rather than data fitting, the aforementioned unsupervised training framework cannot be directly applied.

To address this challenge, we adopt a supervised learning (SL) paradigm inspired by DIFUSCO [43]. Theoretically, the optimal distribution that maximizes the expected utility is a Dirac delta function  $q(\mathbf{x}|\tilde{\mathbf{H}}) = \delta(\mathbf{x} - \mathbf{x}^*(\tilde{\mathbf{H}}))$ , which puts all

### Algorithm 3 SL Training of Conditional Discrete Diffusion

- Require:** Dataset  $\mathcal{D}_{\text{sl}}$ , learning rate  $\zeta$ , transitions  $\{\bar{\mathbf{Q}}_t\}_{t=1}^T$ .
- 1: **repeat**
  - 2:   Sample a pair  $(\tilde{\mathbf{H}}, \mathbf{x}_{\text{AO}}^*)$  from  $\mathcal{D}_{\text{sl}}$
  - 3:   Sample  $t \sim \mathcal{U}\{1, \dots, T\}$
  - 4:   Sample  $\mathbf{x}_t \sim q(\mathbf{x}_t|\mathbf{x}_{\text{AO}}^*) = \text{Cat}(\mathbf{x}_t; \mathbf{p} = \tilde{\mathbf{x}}_{\text{AO}}^* \bar{\mathbf{Q}}_t)$
  - 5:   Compute  $\mathcal{L}_{\text{BCE}} = - \sum_{n=1}^N \log p_\varphi(\hat{x}_{0,n} = x_{\text{AO},n}^*|\mathbf{x}_t, \tilde{\mathbf{H}})$
  - 6:   Update network parameters:  $\varphi \leftarrow \varphi - \zeta \nabla_\varphi \mathcal{L}_{\text{BCE}}$
  - 7: **until** convergence

probability mass on the global optimum  $\mathbf{x}^*(\tilde{\mathbf{H}})$  for a given  $\tilde{\mathbf{H}}$ . As a result, the original objective can be reformulated as minimizing the KL divergence between this optimal delta distribution and our learned distribution, i.e.,

$$\arg \min_{\varphi} \mathbb{E}_{\tilde{\mathbf{H}} \sim p(\tilde{\mathbf{H}})} \left[ D_{\text{KL}} \left( \delta(\mathbf{x} - \mathbf{x}^*(\tilde{\mathbf{H}})) \| p_\varphi(\mathbf{x}|\tilde{\mathbf{H}}) \right) \right], \quad (49)$$

which equivalently reduces to maximizing the log-likelihood of the optimal solutions:

$$\arg \min_{\varphi} \mathbb{E}_{\tilde{\mathbf{H}} \sim p(\tilde{\mathbf{H}})} \left[ - \log p_\varphi(\mathbf{x}^*(\tilde{\mathbf{H}})|\tilde{\mathbf{H}}) \right]. \quad (50)$$

This formulation enables us to employ the previously derived surrogate  $\mathcal{L}_{\text{BCE}}$  for training.

However, obtaining the exact global optimum  $\mathbf{x}^*$  for large-scale FAS is computationally prohibitive due to its NP-hard nature. Instead, we resort to sub-optimal training pairs  $(\tilde{\mathbf{H}}, \mathbf{x}_{\text{AO}}^*)$  obtained via an AO heuristic solver [27]. Specifically, to form the  $i$ -th data pair, we construct  $\tilde{\mathbf{H}}^{(i)}$  by randomly sampling  $K$  individual channels from  $\mathcal{D}_{\text{train}}$  and concatenating them according to (6). Given  $\tilde{\mathbf{H}}^{(i)}$ , the AO algorithm starts with a random initialization of  $M$  active ports and iteratively updates each port via exhaustive search while keeping the remaining  $M - 1$  ports fixed. This procedure repeats until convergence, yielding a locally optimal reference solution  $\mathbf{x}_{\text{AO}}^{*(i)}$ . By repeating this process  $N_{\text{sl}}$  times, we collect the supervised dataset  $\mathcal{D}_{\text{sl}} = \{(\tilde{\mathbf{H}}^{(i)}, \mathbf{x}_{\text{AO}}^{*(i)})\}_{i=1}^{N_{\text{sl}}}$ . Algorithm 3 summarizes the overall SL training procedure.

### C. Reinforcement Fine-tuning

Under the alternative objective (50), the SL-trained model merely tries to “resemble” the AO solutions rather than truly maximizing the original expected utility. Therefore, its performance is upper-bounded by this sub-optimal heuristic baseline. Fortunately, the non-deterministic nature of our learned distribution  $p_\varphi(\mathbf{x}|\tilde{\mathbf{H}})$  facilitates a broader exploration of the combinatorial search space. This inherent stochasticity motivates us to use a reinforcement learning (RL) strategy to fine-tune the SL-established foundation model.

Viewing the port selection process as a single-step RL problem, we define the state as the multiuser channel  $\tilde{\mathbf{H}}$  and the action as the generated mask  $\mathbf{x} \in \{0, 1\}^N$ . Setting the reward directly to the utility  $r(\mathbf{x}, \tilde{\mathbf{H}}) = U(\mathbf{x}, \tilde{\mathbf{H}})$ , the RL objective coincides with (41):

$$J(\varphi) = \mathbb{E}_{\tilde{\mathbf{H}} \sim q(\tilde{\mathbf{H}}), \mathbf{x} \sim p_\varphi(\cdot|\tilde{\mathbf{H}})} \left[ r(\mathbf{x}, \tilde{\mathbf{H}}) \right]. \quad (51)$$

Directly optimizing  $J(\varphi)$  via backpropagation is prohibited by the non-differentiable top- $M$  selection operation at the final generation step. To circumvent this, we adopt the Monte Carlo

Policy Gradient method, which utilizes the log-derivative trick to derive a tractable gradient for training. To stabilize the gradient estimation, we introduce the sub-optimal AO reward as a robust baseline  $b(\tilde{\mathbf{H}}) = r(\mathbf{x}_{\text{AO}}^*, \tilde{\mathbf{H}})$ , yielding the advantage function  $A(\mathbf{x}, \tilde{\mathbf{H}}) = r(\mathbf{x}, \tilde{\mathbf{H}}) - b(\tilde{\mathbf{H}})$ . Overall, the policy gradient is given by

$$\nabla_{\varphi} J(\varphi) = \mathbb{E}_{\tilde{\mathbf{H}}, \mathbf{x}} \left[ A(\mathbf{x}, \tilde{\mathbf{H}}) \nabla_{\varphi} \log p_{\varphi}(\mathbf{x} | \tilde{\mathbf{H}}) \right]. \quad (52)$$

Exploiting the previously established surrogate objective, we approximate the intractable log-likelihood gradient using the BCE loss:  $\nabla_{\varphi} \log p_{\varphi}(\mathbf{x} | \tilde{\mathbf{H}}) \approx -\nabla_{\varphi} \mathcal{L}_{\text{BCE}}(\varphi, \mathbf{x})$ . Substituting this approximation into (52) yields the tractable RL loss:

$$\mathcal{L}_{\text{RL}}(\varphi) \approx \mathbb{E}_{\tilde{\mathbf{H}}, \mathbf{x}} \left[ A(\mathbf{x}, \tilde{\mathbf{H}}) \cdot \mathcal{L}_{\text{BCE}}(\varphi, \mathbf{x}) \right]. \quad (53)$$

In practice, this RL fine-tuning process is implemented via a straightforward self-training loop. For each  $\tilde{\mathbf{H}}$ , we exploit the model's stochasticity to draw  $C$  parallel candidate masks, i.e.,  $\mathbf{x}^{(c)} \sim p_{\varphi}(\cdot | \tilde{\mathbf{H}})$  for  $c \in \{1, \dots, C\}$ . We then evaluate their rewards  $r(\mathbf{x}^{(c)}, \tilde{\mathbf{H}})$  to identify the best candidate  $\mathbf{x}^*$ . In particular, a positive advantage, i.e.,  $r(\mathbf{x}^*, \tilde{\mathbf{H}}) > b(\tilde{\mathbf{H}})$ , indicates the discovery of a solution superior to the AO baseline. Thus, we treat  $\mathbf{x}^*$  as the new ground truth label and update the network by minimizing  $\mathcal{L}_{\text{BCE}}(\varphi, \mathbf{x}^*)$ . This iterative "explore-and-update" mechanism continuously drives the learned model to outperform the AO baseline.

#### D. Online Port Selection and Complexity Analysis

Once the offline training pipeline is complete, the model can be deployed online for port selection given any estimated multiuser channel  $\tilde{\mathbf{H}}$  from Stage I. Since the neural network directly predicts the clean data distribution from any  $\mathbf{x}_t$ , we can accelerate the inference process via skipped sampling, rather than sampling the entire reverse process in (42). Specifically, we define a shortened sub-sequence  $\{\tau_i\}_{i=0}^{T'}$  ( $T' \ll T$ ) where  $\tau_{T'} = T$  and  $\tau_0 = 0$ . Similar to (45), for any intermediate step (i.e.,  $i > 1$ ), the reverse transition from  $\mathbf{x}_{\tau_i}$  to  $\mathbf{x}_{\tau_{i-1}}$  follows

$$p_{\varphi}(\mathbf{x}_{\tau_{i-1}} | \mathbf{x}_{\tau_i}, \hat{\mathbf{H}}) = \sum_{\hat{\mathbf{x}}_0} q(\mathbf{x}_{\tau_{i-1}} | \mathbf{x}_{\tau_i}, \hat{\mathbf{x}}_0) p_{\varphi}(\hat{\mathbf{x}}_0 | \mathbf{x}_{\tau_i}, \hat{\mathbf{H}}). \quad (54)$$

At the final step, we apply a deterministic top- $M$  selection (denoted by  $\arg \text{top}_M$ ) on the predicted  $\hat{\mathbf{x}}_0$  probabilities instead of stochastic sampling. This guarantees that the final selected ports satisfy the FAS hardware constraint. The complete online port selection process is summarized in Algorithm 4.

Owing to the shared U-Net backbone with the Stage I channel estimator, a single forward pass demands the same  $\mathcal{O}(NC_{\text{max}}^2)$  FLOPs established in Section III-D. Since the skipped reverse sampling process in Algorithm 4 involves  $T'$  such evaluations, the overall complexity of the proposed port selector is given by  $\mathcal{O}(T' \cdot N \cdot C_{\text{max}}^2)$ .

## V. NUMERICAL RESULTS

In this section, we present numerical results to evaluate the performance of the proposed unified two-stage diffusion framework for multiuser MIMO-FAS. We begin by detailing the simulation and training setups. We then validate the effectiveness of the Stage I channel estimator in terms of accuracy

---

#### Algorithm 4 Online Port Selection via Discrete Diffusion

---

**Require:** Estimated channel  $\hat{\mathbf{H}}$ , trained model  $p_{\varphi}(\hat{\mathbf{x}}_0 | \mathbf{x}_t, \hat{\mathbf{H}})$ , sampling trajectory  $\{\tau_i\}_{i=1}^{T'}$ .

- 1: Initialize  $\mathbf{x}_{\tau_{T'}} \sim \text{Uniform}(\{0, 1\}^N)$
- 2: **for**  $i = T'$  **to** 1 **do**
- 3:   Compute  $\mathbf{p}_0 = p_{\varphi}(\hat{\mathbf{x}}_0 | \mathbf{x}_{\tau_i}, \hat{\mathbf{H}})$  via the trained model
- 4:   **if**  $i > 1$  **then**
- 5:     Sample  $\mathbf{x}_{\tau_{i-1}} \sim p_{\varphi}(\mathbf{x}_{\tau_{i-1}} | \mathbf{x}_{\tau_i}, \hat{\mathbf{H}})$  given by (54)
- 6:   **else**
- 7:     Construct  $\hat{\mathbf{x}}$  by setting  $\hat{x}_n = 1$  for  $n \in \arg \text{top}_M(\mathbf{p}_0)$  and  $\hat{x}_n = 0$  otherwise
- 8:   **end if**
- 9: **end for**
- 10: **return** Port selection strategy  $\hat{\mathbf{x}}$

---

and robustness, before demonstrating the system-level gains achieved by integrating both stages of the framework.

#### A. Simulation Setup

We consider a narrowband system at carrier frequency  $f_c = 3$  GHz. The BS FAS panel occupies a  $3\lambda \times 3\lambda$  area and is uniformly quantized into  $N = 25 \times 25 = 625$  ports with an ultra-dense spacing of  $d = \lambda/8$ . The BS is equipped with  $M = 4$  active RF chains to serve  $K = 4$  single-FPA users. The BS FAS panel is deployed at a height of 4.0 m, while the  $K$  users at 1.5 m are randomly distributed around the BS with radial distances uniformly drawn from 10 m to 50 m. Multiuser channels are generated using the QuaDRiGa simulator [44] under the 3GPP\_38.901\_Indoor\_NLOS scenario. Each channel realization comprises  $N_p = 20$  dominant paths, characterized by average azimuth and elevation angle spreads of  $72.9^\circ$  and  $24.4^\circ$ , respectively. Furthermore, essential small-scale fading parameters, including path delays, gains, and cluster distributions, are dynamically generated according to the 3GPP standard [45].

A total of 41,000 independent channel realizations are generated via the QuaDRiGa simulator and subsequently normalized to unit variance to facilitate network training. We partition these into a training set  $\mathcal{D}_{\text{train}} = \{\mathbf{h}^{(i)}\}_{i=1}^{40,000}$  for learning the flow-based prior, and a testing set  $\mathcal{D}_{\text{test}}$  of 1,000 samples for downstream evaluation. To initialize the discrete diffusion-based port selector, we further construct a paired dataset  $\mathcal{D}_{\text{sl}} = \{(\tilde{\mathbf{H}}^{(i)}, \mathbf{x}_{\text{AO}}^{*(i)})\}_{i=1}^{N_{\text{sl}}}$  according to the procedure outlined in Section IV-B to pre-train a robust foundation model via SL. The discrete diffusion process utilizes  $T = 500$  steps with a cosine noise schedule [46]. Both the flow-based prior and the SL foundation model are trained for 100 epochs using the Adam optimizer with a learning rate of  $\zeta = 10^{-4}$ . Finally, to surpass the sub-optimal heuristic baseline, the SL foundation model undergoes an additional 100 epochs of RL fine-tuning, as detailed in Section IV-C.

#### B. Impact of Sampling Steps on Channel Estimation Accuracy

For the Stage I channel estimation evaluations, unless otherwise specified, we fix the number of observed ports to  $N_{\mathcal{O}} = 121$  and the signal-to-noise ratio (SNR) at 20 dB. The orthogonal pilot codebook  $\mathbf{P}$  is deterministically constructed

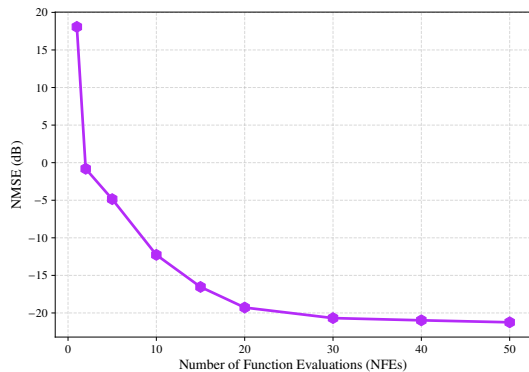


Fig. 4. NMSE of the proposed channel estimator under different NFEs.

from a Hadamard matrix. The estimation accuracy is measured by the normalized mean square error (NMSE), defined as

$$\text{NMSE} = \mathbb{E} \left[ \frac{\|\hat{\mathbf{H}} - \tilde{\mathbf{H}}\|_F^2}{\|\tilde{\mathbf{H}}\|_F^2} \right], \quad (55)$$

where  $\tilde{\mathbf{H}}$  and  $\hat{\mathbf{H}}$  represent the ground-truth and estimated multiuser channel matrices, respectively. Given that the generated channel samples are normalized, the SNR simplifies to  $\text{SNR} = 1/\sigma_n^2$ . Furthermore, for the proposed flow-based channel estimator detailed in Algorithm 2, the number of guidance iterations is set to  $N_{\text{iter}} = 3$ , with a fixed gradient step size of  $\alpha_t = 50$ .

Fig. 4 illustrates the NMSE performance of the proposed flow-based channel estimator against the NFEs. The results demonstrate a sharp reduction in NMSE as the NFE increases from a highly coarse sampling grid, before quickly stabilizing at an NFE of around 20. This indicates that a denser sampling trajectory (i.e., a larger NFE) yields marginal estimation gains at the expense of a proportional increase in inference latency. This rapid saturation demonstrates the promising potential of our flow-based generative approach for real-time, high-dimensional multiuser FAS channel estimation.

### C. Robustness of Channel Estimation Across SNR Regimes

For fair comparisons with existing FAS channel estimation techniques, which are primarily designed for SISO-FAS scenarios, we first decouple the multiuser channel estimation problem into  $K$  individual SISO recovery tasks. This is achieved by right-multiplying the observations in (3) by the pilot pseudo-inverse, i.e.,  $\mathbf{Y}_p \mathbf{P}^\dagger$ . If full array observation is available ( $N_{\mathcal{O}} = N$ ), this least squares (LS) estimator can directly serve as a fundamental performance benchmark. For practical sub-sampled recovery scenarios ( $N_{\mathcal{O}} < N$ ), we evaluate three baselines:

- **OMP**: The classical Orthogonal Matching Pursuit (OMP) algorithm exploits the inherent channel sparsity of  $\hat{\mathbf{h}}_k$  in the angular domain, where we construct an over-complete dictionary with a resolution of  $G = 50$  grids for both azimuth and elevation AoAs.
- **SBL**: The Sparse Bayesian Learning (SBL) method proposed in [18] utilizes the expectation-maximization (EM) algorithm to learn a parameterized Gaussian prior over the sparse angular representation of  $\hat{\mathbf{h}}_k$  based on the same

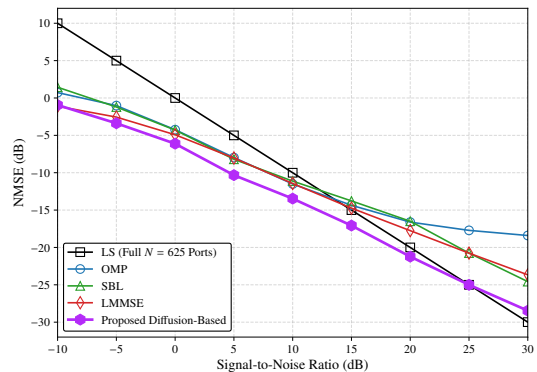


Fig. 5. NMSE performance versus SNR.

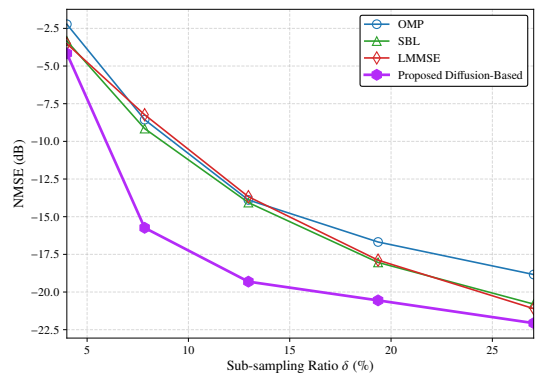


Fig. 6. NMSE performance versus sub-sampling ratio  $\delta$ .

dictionary as OMP.

- **LMMSE**: The Linear Minimum Mean Square Error (LMMSE) estimator assumes a simplified Gaussian prior  $\mathbf{h}_k \sim \mathcal{CN}(\mathbf{0}, \mathbf{R}_h)$ , where the covariance matrix  $\mathbf{R}_h$  is empirically computed from the 40,000 training samples.

Fig. 5 illustrates the NMSE comparison for SNRs from  $-10$  to  $30$  dB. Although the full-observation LS estimator achieves competitive accuracy at high SNRs, it requires a prohibitive switching overhead across all  $N$  ports. In contrast, the proposed flow-based estimator significantly outperforms all sub-sampled baselines across the entire evaluated SNR regime. These performance gaps further widen under more restrictive observations, as elaborated in the following subsection.

### D. Impact of Sub-sampling Ratio

To further investigate the channel estimation performance under severely observation-limited conditions, we evaluate the NMSE against varying sub-sampling ratios  $\delta = N_{\mathcal{O}}/N$  at a fixed SNR = 20 dB. The LS estimator is excluded from this evaluation since it requires full array observation, i.e.,  $\delta = 100\%$ . Fig. 6 reveals a substantial performance gap in the severely under-sampled regime. Specifically, as  $\delta$  increases from 4% to 10%, our flow-based estimator exhibits a rapid NMSE drop, significantly outperforming all other baselines.

We attribute this remarkable performance gain to the fact that our flow-based channel estimator implicitly learns the intricate true prior distribution of the FAS channels, enabling robust reconstruction even from severely limited spatial observations. In contrast, CS-based schemes (OMP and SBL) suffer

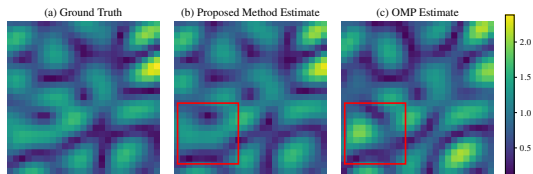


Fig. 7. Visual comparison of estimated channel magnitudes (SNR = 20 dB,  $\delta \approx 8\%$ ). Red boxes highlight structural estimation errors in the OMP baseline, which are effectively mitigated by the proposed method.

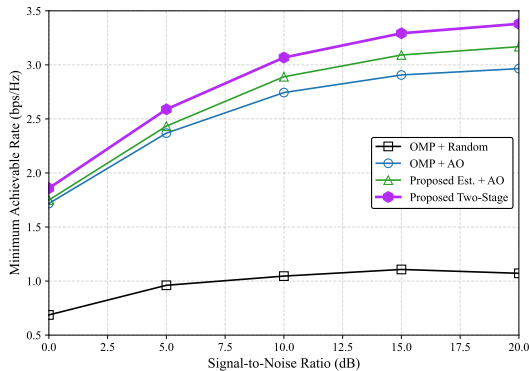


Fig. 8. Minimum Achievable Rate versus SNR.

from highly ill-conditioned measurement matrices at low subsampling ratios, preventing them from accurately resolving the sparse angular paths. In addition, the LMMSE approach relies on an over-simplified Gaussian prior that is insufficient for faithful recovery under limited observations.

To provide deeper insights into the reconstruction quality, Fig. 7 presents a visual comparison of the estimated channels for a representative user at SNR = 20 dB and  $\delta \approx 8\%$ . As highlighted by the red boxes, the OMP estimate exhibits significant structural estimation errors, while the proposed channel estimator faithfully recovers the true spatial variations. Beyond numerical accuracy, preserving this spatial pattern integrity is also critical, since any structural artifact will inevitably mislead the downstream port selection, ultimately resulting in a severe degradation of the achievable capacity.

#### E. Minimum Achievable Rate With Estimated Channel

Finally, Fig. 8 evaluates the overall system-level performance by plotting the minimum achievable rate versus SNR, where the Stage I estimated channels are directly fed into Stage II port selection. This evaluation aims to inspect the cascading effect of the plug-in approximation established in Section II-C, as estimation errors propagate directly into the downstream port selection stage. An ablation study is conducted by comparing four scheme combinations:

- **OMP + Random:** Channel estimation via OMP, followed by randomly selecting  $M = 4$  active ports.
- **OMP + AO:** Channel estimation via OMP, followed by port selection using the existing AO heuristic solver [27].
- **Proposed Est. + AO:** Channel estimation via our proposed flow-based estimator, while the downstream port selection is done by the AO heuristic solver.
- **Proposed Two-Stage:** Our complete unified two-stage diffusion framework, which utilizes the flow-based es-

TABLE I  
STAGE I COMPUTATIONAL COMPLEXITY COMPARISON

Algorithm	Computational Complexity
OMP	$\mathcal{O}(K \cdot I_{\text{OMP}} \cdot \delta N G^2)$
SBL [18]	$\mathcal{O}(K \cdot I_{\text{SBL}} \cdot (\delta^2 N^2 G^2 + \delta^3 N^3))$
LMMSE	$\mathcal{O}(K \cdot (\delta^3 N^3 + \delta N^2))$
<b>Proposed</b>	$\mathcal{O}(\text{NFE} \cdot N \cdot (K C_{\text{max}}^2 + N_{\text{iter}} \delta K^2))$

TABLE II  
STAGE II COMPUTATIONAL COMPLEXITY COMPARISON

Algorithm	Computational Complexity
AO [27]	$\mathcal{O}(I_{\text{AO}} \cdot M(N - M) \cdot (MK + K^2))$
<b>Proposed</b>	$\mathcal{O}(T' \cdot N \cdot C_{\text{max}}^2)$

imator for channel estimation and the RL-fine-tuned discrete diffusion-based port selector.

As shown in Fig. 8, the proposed two-stage framework consistently achieves the highest minimum achievable rate across all evaluated SNRs. This gain demonstrates how our proposed framework mitigates the two compounded error sources inherent in the plug-in approximation. First, unlike OMP + AO, the proposed flow-based estimator effectively eliminates structural estimation errors, providing a faithful channel proxy that restricts downstream error propagation. Second, compared to Proposed Est. + AO, our discrete diffusion model avoids the poor local optima that trap traditional AO algorithms. These results confirm that the plug-in approximation error is significantly suppressed, validating our framework as a tractable surrogate for the joint MAP objective in (15).

#### F. Complexity Comparison

Tables I and II compare the per-stage computational complexity of the proposed framework with baselines, where  $I_{\text{OMP}}$ ,  $I_{\text{SBL}}$ , and  $I_{\text{AO}}$  denote the iteration counts of OMP, SBL, and AO, respectively. Notably, the proposed Stage I estimator scales linearly with  $N$ , matching OMP while bypassing the prohibitive  $\mathcal{O}(N^3)$  matrix inversion bottleneck of SBL and LMMSE. This efficient  $\mathcal{O}(N)$  scaling also extends to Stage II. Crucially, while both methods scale linearly with  $N$ , our approach completely eliminates AO's dependency on the active port count  $M$  due to exhaustive search. Consequently, the unified two-stage framework exhibits highly favorable scalability behavior, making it well suited for large-scale multiuser MIMO-FAS deployments.

## VI. CONCLUSION

In this paper, we proposed a unified two-stage diffusion framework to solve the fundamental challenges of channel estimation and port selection in multiuser MIMO-FAS. By casting the joint task as a single MAP inference problem and decomposing it via a plug-in approximation, the proposed framework establishes a principled probabilistic bridge between the two stages, realized by a flow-based channel posterior sampler and a discrete diffusion port selector. Numerical results confirm that our framework achieves substantial gains in the minimum achievable rate over conventional decoupled baselines, driven by its exceptional robustness against severely sub-sampled pilots and realistic estimation errors. In summary, this work

establishes generative diffusion models as a compelling solution for tackling high-dimensional, non-convex physical-layer challenges, offering a practical and scalable methodology for large-scale MIMO-FAS deployments.

## REFERENCES

- [1] K. B. Letaief, Y. Shi, J. Lu, and J. Lu, "Edge artificial intelligence for 6G: Vision, enabling technologies, and applications," *IEEE J. Sel. Areas Commun.*, vol. 40, no. 1, pp. 5–36, Jan. 2022.
- [2] W. Saad, M. Bennis, and M. Chen, "A vision of 6G wireless systems: Applications, trends, technologies, and open research problems," *IEEE Netw.*, vol. 34, no. 3, pp. 134–142, May 2020.
- [3] C.-X. Wang *et al.*, "On the road to 6G: Visions, requirements, key technologies, and testbeds," *IEEE Commun. Surveys Tuts.*, vol. 25, no. 2, pp. 905–974, 2nd Quart. 2023.
- [4] Z. Wang *et al.*, "A tutorial on extremely large-scale MIMO for 6G: Fundamentals, signal processing, and applications," *IEEE Commun. Surveys Tuts.*, vol. 26, no. 3, pp. 1560–1605, 3rd Quart. 2024.
- [5] A. Shojaiefard *et al.*, "MIMO evolution beyond 5G through reconfigurable intelligent surfaces and fluid antenna systems," *Proc. IEEE*, vol. 110, no. 9, pp. 1244–1265, Sep. 2022.
- [6] K.-K. Wong, K.-F. Tong, Y. Zhang, and Z. Zhongbin, "Fluid antenna system for 6G: When Bruce Lee inspires wireless communications," *IET Electron. Lett.*, vol. 56, no. 24, pp. 1288–1290, Nov. 2020.
- [7] K.-K. Wong, A. Shojaiefard, K.-F. Tong, and Y. Zhang, "Fluid antenna systems," *IEEE Trans. Wireless Commun.*, vol. 20, no. 3, pp. 1950–1962, Mar. 2021.
- [8] K. K. Wong, A. Shojaiefard, K.-F. Tong, and Y. Zhang, "Performance limits of fluid antenna systems," *IEEE Commun. Lett.*, vol. 24, no. 11, pp. 2469–2472, Nov. 2020.
- [9] W. K. New, K.-K. Wong, H. Xu, K.-F. Tong, and C.-B. Chae, "Fluid antenna system: New insights on outage probability and diversity gain," *IEEE Trans. Wireless Commun.*, vol. 23, no. 1, pp. 128–140, Jan. 2024.
- [10] L. Tlebaldiyeva, S. Arzykulov, K. M. Rabie, X. Li, and G. Naurzybayev, "Outage performance of fluid antenna system (FAS)-aided terahertz communication networks," in *Proc. IEEE Int. Conf. Commun. (ICC)*. IEEE, 2023, pp. 1922–1927.
- [11] M. Khammassi, A. Kammoun, and M.-S. Alouini, "A new analytical approximation of the fluid antenna system channel," *IEEE Trans. Wireless Commun.*, vol. 22, no. 12, pp. 8843–8858, Dec. 2023.
- [12] C. Wang *et al.*, "Fluid antenna system liberating multiuser MIMO for ISAC via deep reinforcement learning," *IEEE Trans. Wireless Commun.*, vol. 23, no. 9, pp. 10879–10894, Sep. 2024.
- [13] W. K. New, K.-K. Wong, H. Xu, K.-F. Tong, and C.-B. Chae, "An information-theoretic characterization of MIMO-FAS: Optimization, diversity-multiplexing tradeoff and q-outage capacity," *IEEE Trans. Wireless Commun.*, vol. 23, no. 6, pp. 5541–5556, Jun. 2024.
- [14] L. Zhu, W. Ma, and R. Zhang, "Movable-antenna array enhanced beamforming: Achieving full array gain with null steering," *IEEE Commun. Lett.*, vol. 27, no. 12, pp. 3340–3344, Dec. 2023.
- [15] W. K. New *et al.*, "A tutorial on fluid antenna system for 6G networks: Encompassing communication theory, optimization methods and hardware designs," *IEEE Commun. Surveys Tuts.*, vol. 27, no. 4, pp. 2325–2377, Aug. 2025.
- [16] W. Ma, L. Zhu, and R. Zhang, "Compressed sensing based channel estimation for movable antenna communications," *IEEE Commun. Lett.*, vol. 27, no. 10, pp. 2747–2751, Oct. 2023.
- [17] Z. Xiao *et al.*, "Channel estimation for movable antenna communication systems: A framework based on compressed sensing," *IEEE Trans. Wireless Commun.*, vol. 23, no. 9, pp. 11814–11830, Sep. 2024.
- [18] B. Xu, Y. Chen, Q. Cui, X. Tao, and K.-K. Wong, "Sparse Bayesian learning-based channel estimation for fluid antenna systems," *IEEE Wireless Commun. Lett.*, vol. 14, no. 2, pp. 325–329, Feb. 2025.
- [19] C. Skouroumounis and I. Krikidis, "Fluid antenna with linear MMSE channel estimation for large-scale cellular networks," *IEEE Trans. Commun.*, vol. 71, no. 2, pp. 1112–1125, Feb. 2023.
- [20] Z. Zhang, J. Zhu, L. Dai, and R. W. Heath, "Successive Bayesian reconstructor for channel estimation in fluid antenna systems," *IEEE Trans. Wireless Commun.*, vol. 24, no. 3, pp. 1992–2006, Mar. 2025.
- [21] Z. Chen, J. Li, X. Y. Zhang, K.-K. Wong, C.-B. Chae, and Y. Zhang, "Iterative sparse asymptotic minimum variance based channel estimation in fluid antenna system," *arXiv preprint arXiv:2507.05625*, 2025.
- [22] H. Guo, J. Zhang, J. Rao, R. Murch, and V. K. Lau, "Channel estimation and analog precoding for pixel-based fluid-antenna-assisted multiuser MIMO-OFDM systems," *arXiv preprint arXiv:2509.09373*, 2025.
- [23] H. Xu *et al.*, "Channel estimation for FAS-assisted multiuser mmWave systems," *IEEE Commun. Lett.*, vol. 28, no. 3, pp. 632–636, Mar. 2024.
- [24] H. Qin, W. Chen, Z. Li, Q. Wu, N. Cheng, and F. Chen, "Antenna positioning and beamforming design for fluid antenna-assisted multi-user downlink communications," *IEEE Wireless Commun. Lett.*, vol. 13, no. 4, pp. 1073–1077, Apr. 2024.
- [25] Z. Cheng, N. Li, J. Zhu, X. She, C. Ouyang, and P. Chen, "Sum-rate maximization for fluid antenna enabled multiuser communications," *IEEE Commun. Lett.*, vol. 28, no. 5, pp. 1206–1210, May 2024.
- [26] T. Liao, W. Guo, H. He, S. Song, J. Zhang, and K. B. Letaief, "Joint beamforming and antenna position optimization for fluid antenna-assisted MU-MIMO networks," *IEEE J. Sel. Areas Commun.*, vol. 44, pp. 1209–1226, Sep. 2025.
- [27] Z. Cheng, N. Li, J. Zhu, C. Ouyang, and X. Zhang, "Exploiting movable antennas in multicast communications," *arXiv preprint arXiv:2405.07281*, 2024.
- [28] Z. Xiao, X. Pi, L. Zhu, X.-G. Xia, and R. Zhang, "Multiuser communications with movable-antenna base station: Joint antenna positioning, receive combining, and power control," *IEEE Trans. Wireless Commun.*, vol. 23, no. 12, pp. 19744–19759, Dec. 2024.
- [29] Y. Wu, D. Xu, D. W. K. Ng, W. Gerstacker, and R. Schober, "Globally optimal movable antenna-enabled multiuser communication: Discrete antenna positioning, power consumption, and imperfect CSI," *IEEE Trans. Commun.*, vol. 73, no. 10, pp. 9903–9923, Oct. 2025.
- [30] L. N. Pringle *et al.*, "A reconfigurable aperture antenna based on switched links between electrically small metallic patches," *IEEE Trans. Antennas Propag.*, vol. 52, no. 6, pp. 1434–1445, Jun. 2004.
- [31] A. Zhuravlev, V. Razevig, S. Ivashov, A. Bugaev, and M. Chizh, "Experimental simulation of multi-static radar with a pair of separated movable antennas," in *Proc. IEEE COMCAS*. IEEE, 2015, pp. 1–5.
- [32] J. Zhang *et al.*, "A novel pixel-based reconfigurable antenna applied in fluid antenna systems with high switching speed," *IEEE Open J. Antennas Propag.*, vol. 6, no. 1, pp. 212–228, Feb. 2025.
- [33] R. T. Chen, Y. Rubanova, J. Bettencourt, and D. K. Duvenaud, "Neural ordinary differential equations," *Proc. Advances in Neural Information Processing Systems (NeurIPS)*, vol. 31, 2018.
- [34] Y. Lipman, R. T. Chen, H. Ben-Hamu, M. Nickel, and M. Le, "Flow matching for generative modeling," *arXiv preprint arXiv:2210.02747*, 2022.
- [35] M. S. Albergo and E. Vanden-Eijnden, "Building normalizing flows with stochastic interpolants," *arXiv preprint arXiv:2209.15571*, 2022.
- [36] X. Liu, C. Gong, and Q. Liu, "Flow straight and fast: Learning to generate and transfer data with rectified flow," *arXiv preprint arXiv:2209.03003*, 2022.
- [37] J. Kim, B. S. Kim, and J. C. Ye, "FlowDPS: Flow-driven posterior sampling for inverse problems," in *Proc. IEEE/CVF Int. Conf. Comput. Vis. (ICCV)*, 2025, pp. 12328–12337.
- [38] D. Tse and P. Viswanath, *Fundamentals of wireless communication*. Cambridge Univ. Press, 2005.
- [39] E. Tang, W. Guo, H. He, S. Song, J. Zhang, and K. B. Letaief, "Accurate and fast channel estimation for fluid antenna systems with diffusion models," in *Proc. IEEE Global Commun. Conf. (GLOBECOM)*, Dec. 2025, pp. 2066–2071.
- [40] H. Chung, J. Kim, M. T. Mccann, M. L. Klasky, and J. C. Ye, "Diffusion posterior sampling for general noisy inverse problems," *arXiv preprint arXiv:2209.14687*, 2022.
- [41] J. Austin, D. D. Johnson, J. Ho, D. Tarlow, and R. Van Den Berg, "Structured denoising diffusion models in discrete state-spaces," *Proc. Advances in Neural Information Processing Systems (NeurIPS)*, vol. 34, pp. 17981–17993, 2021.
- [42] J. Ho, A. Jain, and P. Abbeel, "Denoising diffusion probabilistic models," *Proc. Advances in Neural Information Processing Systems (NeurIPS)*, vol. 33, pp. 6840–6851, 2020.
- [43] Z. Sun and Y. Yang, "DIFUSCO: Graph-based diffusion solvers for combinatorial optimization," *Proc. Advances in Neural Information Processing Systems (NeurIPS)*, vol. 36, pp. 3706–3731, 2023.
- [44] S. Jaeckel, L. Raschkowski, K. Börner, L. Thiele, F. Burkhardt, and E. Eberlein, "QuaDRiGa—quasi deterministic radio channel generator, user manual and documentation," 2017.
- [45] 3GPP, "Study on channel model for frequencies from 0.5 to 100 GHz," 3rd Generation Partnership Project (3GPP), 3GPP Tech. Rep. 38.901 V17.0.0, Apr. 2022.
- [46] A. Q. Nichol and P. Dhariwal, "Improved denoising diffusion probabilistic models," in *Proc. Int. Conf. Mach. Learn. (ICML)*. PMLR, 2021, pp. 8162–8171.